

ENME 570: Aerodynamics

Final Project Report

Matthew Halas

Affiliation:

Department of Mechanical Engineering

University of Calgary

Calgary, Alberta

1. Abstract

A novel wing, the CVCII, was designed for use in a UAV. The requirements for the wing were a high lift to drag ratio over a range of angles of attack from 0 to 20 degrees, and a high stall angle. The wing was tested experimentally in a wind tunnel, and numerically in ANSYS Fluent. The resulting performance score, as outlined in the project description, was 2.056. In the 2D CFD analysis, the wing stalled at AoA of 16 degrees. The importance of finite wing effects was investigated when comparing the results of the 2D CFD analysis with the experimental and 3D CFD results. Two major highlights of the comparison are the slope of the lift curves and the AoA at maximum lift to drag ratio. The slope of the lift curve in the 2D case was almost two times higher than that of the finite wing cases. This was likely caused by the effect of downwash on the effective angle becoming more significant as lift is increased. The AoA at maximum lift to drag ratio was 16 degrees for the 2D CFD case and 11 and 12 degrees for the experimental and 3D CFD cases respectively. For finite wings, the induced drag is proportional to the lift coefficient squared, resulting in a lower lift to drag ratio as lift is increased past a certain point. When comparing the performance of the CVCII to conventional NACA airfoils, it is found that although the maximum lift is similar to the maximum lift of NACA airfoils, the maximum lift to drag ratio is almost six times lower. This is caused by the large pressure drag from separating flow at the back half of the airfoil. This flow separation occurs at all angles of attack, which is detrimental to the performance of the wing.

Contents

1. Abstract	1
2. Introduction	3
3. Background	4
3.1. Basic Aerodynamics	4
3.2. Finite Wing Effects	6
3.3. Computational Fluid Dynamics	8
3.4. CFD Results.....	9
4. Objectives and Hypothesis.....	10
5. Methodology.....	11
5.1. Modelling and Printing.....	11
5.2. Wind Tunnel Test	12
5.3. 2D CFD.....	12
5.4. 3D CFD.....	14
6. Results and Discussion	16
6.1. Experimental	16
6.2. Computational Fluid Dynamics – 2D Analysis.....	22
6.3. Computational Fluid Dynamics – 3D	30
6.4. Comparison of Results	35
6.5. Comparison with existing airfoil designs	39
6.6. Performance score	41
6.7. Sources of error	41
6.7.1 Experimental Errors	41
6.7.2 CFD Analysis Errors	42
6.8. Improvements.....	42
6.8.1 Experimental	42
6.8.2 CFD	43
6.8.3 Design.....	43
7. Conclusion.....	43
8. References	44

2. Introduction

When analyzing a wing, or its 2D approximation, an airfoil, two of the most important characteristics to look at are its lift and drag. Ideally, a wing will have a high lift to drag ratio. When a wing is placed in a flow-field, i.e., the wing is moving with respect to the surrounding air, it will experience a lift and a drag force. The lift force acts perpendicular to the direction of the oncoming air, and the drag force acts in the direction of the oncoming air. A diagram showing the lift and drag forces on an airfoil is shown in figure 1. A wing with a high lift to drag ratio will require less thrust to stay in flight than a wing with a lower lift to drag ratio.

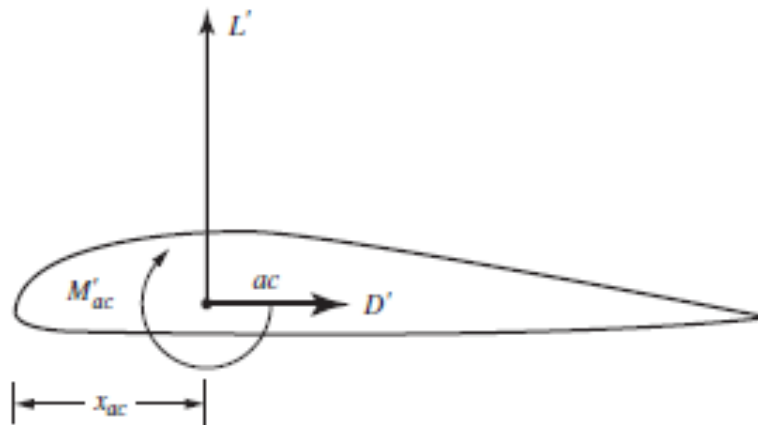


Figure 1: Schematic showing lift, drag, and moment forces on airfoil [1]

In addition to a high lift to drag ratio, a high stall angle may be desirable depending on the application. Stall occurs when the flow going over the top surface of the wing separates, leading to a wake of recirculating air behind the wing. At the point of stall, the lift begins to decrease, and the drag begins to increase drastically. Figure 2 shows the streamlines going over an airfoil during stall.

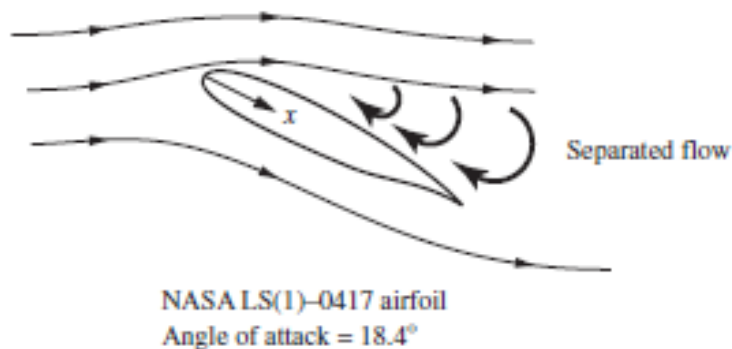


Figure 2: Streamlines over an airfoil experiencing stall [1]

The purpose of this project is to design a high-performance wing for use in a new unmanned aerial vehicle. The two main objectives for the wing are a high lift to drag ratio between an angle of attack (AoA) of 0 degrees to 20 degrees, and a high stall angle. Any new or existing airfoil shape can be used for the profile of the wing. The span, planform area, twist, or any other geometric properties of the wing

can be chosen, if they fit within the specified dimensions. The performance of the new wing will be tested experimentally in a wind tunnel, and numerically through ANSYS Fluent.

For this project, an unconventional wing design was used. The wing was modeled after my car, a 2005 Honda Civic. The profile is shown in figure 3.

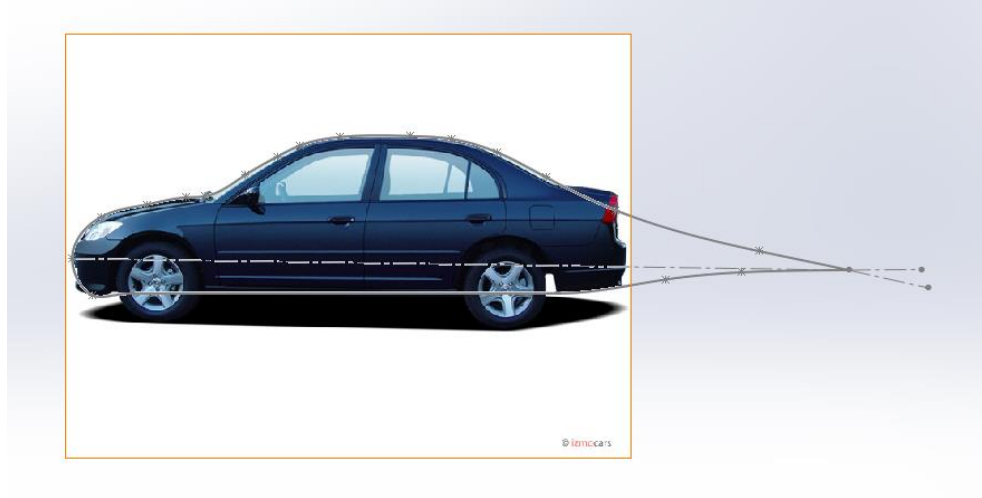


Figure 3: CVCII wing profile with picture of car used to assist with sketch [2]

The rest of the design choices that went into creating the wing will be described in the methodology section. For the remainder of the report, the wing prototype will be referred to as the CVC mk.2, or CVCII.

3. Background

The basic theory used throughout this project will be discussed in this section.

3.1. Basic Aerodynamics

Beginning with some basic aerodynamic definitions, the lift, drag, and moment coefficient are:

$$C_L = \frac{L}{q_\infty S}$$

$$C_D = \frac{D}{q_\infty S}$$

$$C_{M,c/4} = \frac{M_{c/4}}{q_\infty S l}$$

Where L is the lift force in Newtons, S is the planform area, D is the drag force in Newtons, $M_{c/4}$ is the moment about the quarter chord location, and l is the chord length. q_∞ , the dynamic pressure head, is given by:

$$q_\infty = \frac{1}{2} \rho_\infty V_\infty^2$$

Where ρ_∞ is the density and V_∞ is the freestream velocity. These coefficients are useful when comparing the performance of different geometries at different conditions. The aerodynamic center is an important location to consider when analyzing a wing/airfoil. The aerodynamic center is the point along the chord at which the moment coefficient is independent of the AoA. The theoretical lift coefficient can be determined using thin airfoil theory. The derivation is beyond the scope of this report; however, the theoretical slope of the lift curve is $2\pi \text{ rad}^{-1}$ [1]. The theoretical lift is compared to experimental data for the NACA 0012 airfoil in figure 4.

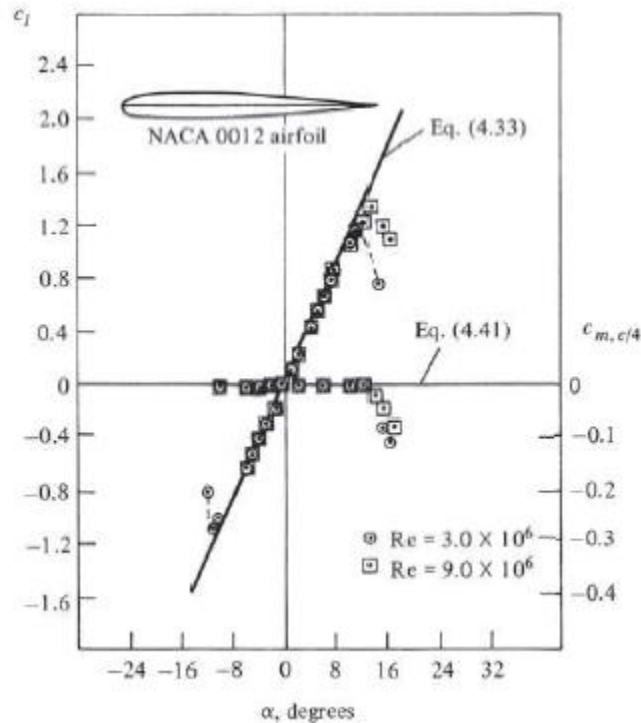


Figure 4: Comparison between experimental and theoretical lift coefficient and moment coefficient for NACA 0012 airfoil [1]

The theoretical lift slope is only valid for relatively thin airfoils. Thicker airfoils may display a shallower lift curve. As an example, the characteristics of two NACA airfoils are observed; the NACA 0015 and NACA 4421. Their profiles are shown in figures 5 and 6.

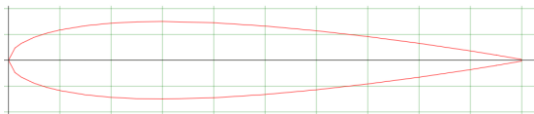


Figure 5: NACA 0015 airfoil profile [3]

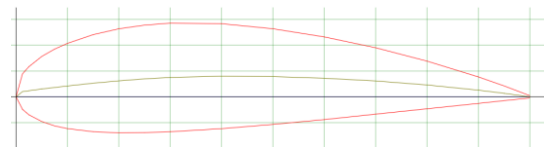


Figure 6: NACA 4421 airfoil profile [3]

The NACA 4421 has a camber and is thicker than the NACA 0015. The lift to drag ratio vs angle of attack for the two airfoils is shown in figure 7.

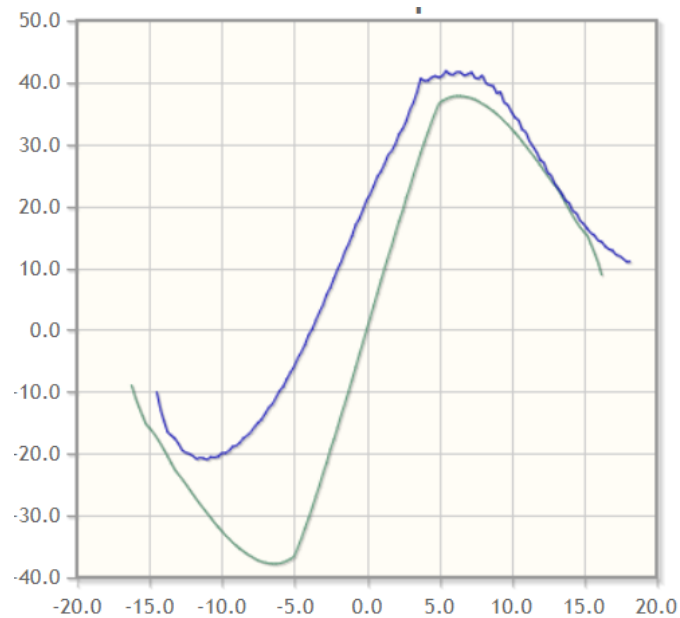


Figure 7: Lift to drag ratio vs AoA for NACA 0015 (Green/lower) and NACA 4421 (Blue/upper) airfoils at $Re=100000$ [3]

The shape of the airfoil can make a drastic difference to the lift and drag characteristics of a wing.

3.2. Finite Wing Effects

In addition to the profile of the wing, the actual shape of the wing, such as the span, chord length, and planform shape is important to consider. An important aerodynamic concept to consider when designing the shape of the wing is downwash. With high-pressure air on the lower surface of the wing, and low-pressure air on the upper surface, air tends to curl up around the tip of the wing, resulting in tip vortices. Figure 8 shows a diagram of tip vortices.

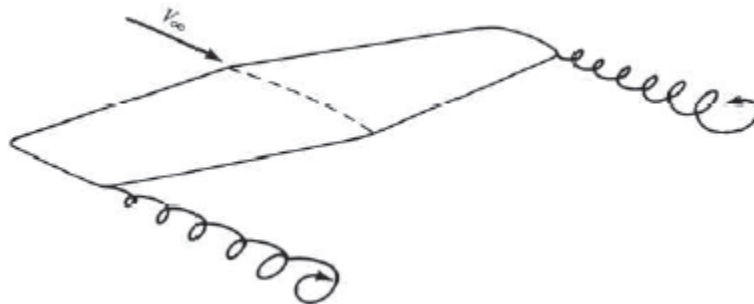


Figure 8: Drawing of tip vortices on a finite wing [1]

A product of these tip vortices is downwash. Downwash created by tip vortices lowers the effective angle of attack of the wing. Figure 9 illustrates the effective angle of attack caused by downwash.

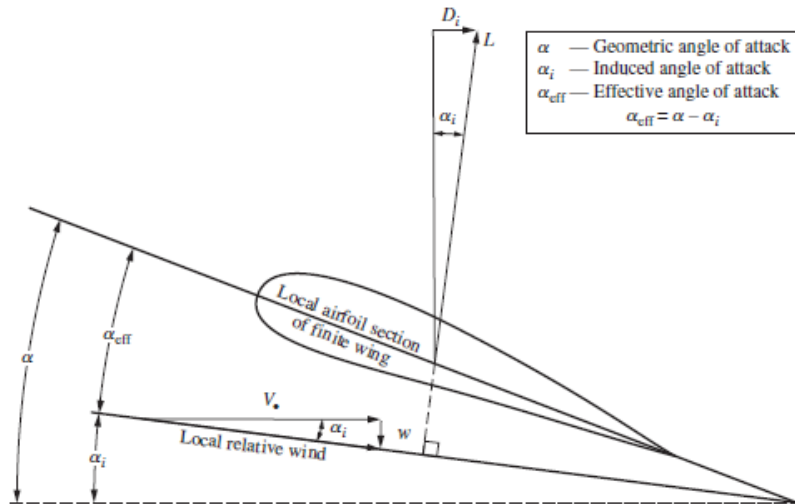


Figure 9: Diagram of effective angle of attack caused by downwash [1]

Downwash introduces an induced drag, D_i , as shown in the diagram above. If the goal of the wing is to maximize the lift to drag ratio, a lower induced drag is desirable. Sparing the derivation, the ideal lift distribution to minimize induced drag is elliptical [1]. This means that for a wing with no geometric or aerodynamic twist, the chord length should be elliptical over the wingspan if the elliptical lift distribution is desired.



Figure 10: The Supermarine Spitfire is a fighter plane with an elliptical wing shape [4]

For an elliptical lift distribution specifically, the induced drag as a function of lift is [1]:

$$C_{D,i} = \frac{C_L^2}{\pi AR}$$

Where $C_{D,i}$ is the induced drag coefficient, and AR is the aspect ratio of the wing.

3.3. Computational Fluid Dynamics

Computational Fluid Dynamics (CFD) will be used to test the effectiveness of the chosen wing. In general, the approach of CFD is to break a continuous domain down into a discrete domain using a mesh or grid. An example of what this grid may look like is shown in figure 11.

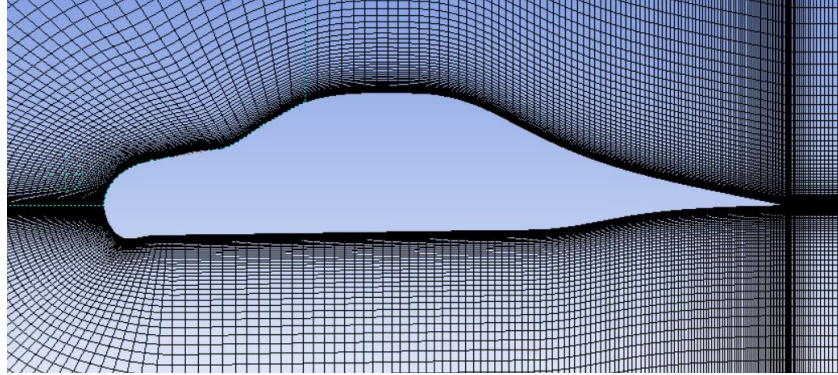


Figure 11: Mesh used for CFD analysis on airfoil

For this analysis, ANSYS Fluent will be used. Fluent is a finite volume method (FVM) solver, meaning that each cell describes a control volume, to which the governing equations can be applied. For this analysis, the incompressible continuity and momentum equations are used. The momentum equation is [5]:

$$\rho \frac{\partial V}{\partial t} + \rho V \cdot \nabla V = -\nabla p + \mu \nabla^2 V$$

And the incompressible continuity equation is:

$$\nabla \cdot V = 0$$

Figure 12 can be used as an example of the application of these equations to a finite volume. In the diagram, each face has an x and y velocity, u and v , as well as a length, Δx or Δy .

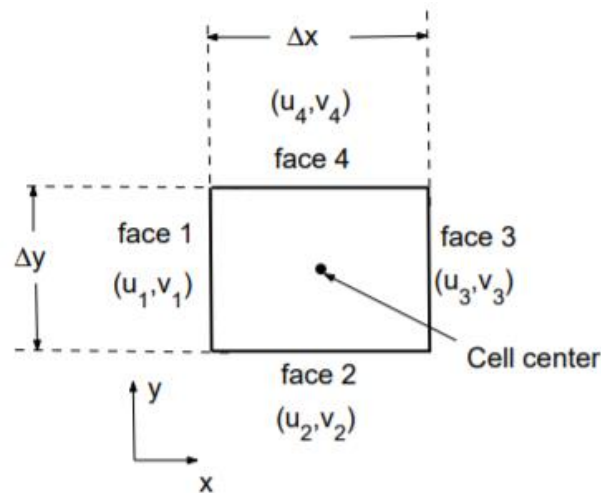


Figure 12: Diagram of a cell in finite volume method CFD [6]

Applying the continuity equation to the cell:

$$\nabla \cdot V = -u_1 \Delta y + u_3 \Delta y - v_2 \Delta x + v_4 \Delta x = 0$$

Only the properties in the center of the cell are directly solved for, however, the properties at the faces are important for calculating the governing equations. The values at the faces are solved by interpolation. Fluent offers several options of interpolating for the face values. They will not be explained in detail here but will be mentioned again in section 5.3.

With the domain discretized and the equations set, boundary and initial conditions can be imposed on the geometry. With the assumption of steady flow, the solver will try to find a steady solution for the problem given the discretized domain and boundary conditions.

Turbulence modeling is an important aspect of CFD. For turbulence to be resolved using the conservation equations, the mesh size would have to be reduced to the smallest turbulent dissipative scales. Due to the computational resources required for a mesh that small, this method is not practical. Instead, models are used to predict turbulence without requiring a reduction in mesh size. The exact mechanics of these turbulence models will not be covered in this report, but the selected turbulence model will be discussed briefly in section 5.3.

3.4. CFD Results

Some background on the results that will be analyzed in the CFD portion of this project will be provided here. One result that will be investigated in detail is the pressure coefficient:

$$C_p = \frac{p - p_\infty}{q_\infty}$$

Where p is the local pressure and p_∞ is the freestream pressure. The ideal pressure coefficient distribution on the surface of an airfoil would be a low pressure on the top surface (suction side) and a high pressure on the lower surface (pressure side).

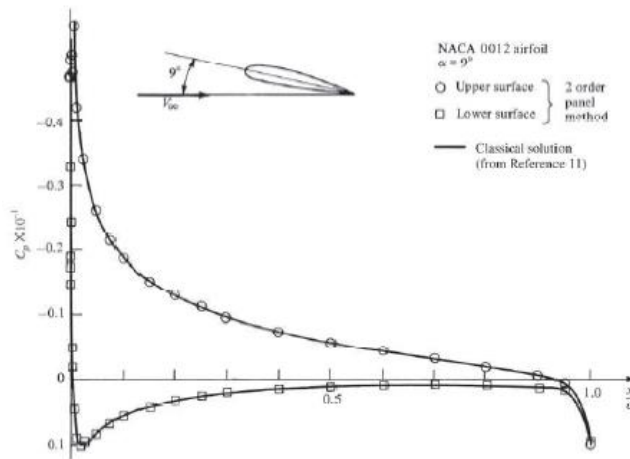


Figure 13: Pressure coefficient distribution over surface of NACA 0012 airfoil [1]

The skin friction coefficient will also be analyzed:

$$C_f = \frac{D}{q_\infty S}$$

Where D is the drag due to skin friction. In addition to skin friction drag, pressure due to flow separation plays a large role in this analysis. Pressure drag due to flow separation arises when flow separates over the back side of a geometry. This results in a low-pressure zone on the back side pushing forward, and a high-pressure zone on the front side pushing back. Because the pressure on the front surface is higher than the back surface, a drag force is experienced.

4. Objectives and Hypothesis

As stated in the introduction, the objective of this project is to build a high-performance wing with a high lift to drag ratio between an AoA of 0 and 20 degrees and a high stall angle. The CVCII wing will be tested in a wind tunnel, in a 2D CFD simulation, and a 3D CFD simulation. All tests will be performed at multiple angles of attack from 0 to 20 degrees.

The performance of the wing will be quantified using a performance score:

$$P = 0.6P_1 + 0.4P_2$$

Where P_1 and P_2 are:

$$P_1 = \frac{1}{v} \int_0^{20} \frac{C_L}{C_D} d\alpha$$

$$P_2 = \frac{\alpha_{stall}}{4}$$

The performance score will be calculated using the results of the 2D CFD analysis.

The chosen wing must also follow the geometric constraints:

- Maximum chord length: 10 cm
- Maximum planform area: 230 cm²
- Minimum wing volume: 60 cm³
- Maximum wing volume: 230 cm³
- Maximum wingspan: 28 cm

Given the unconventional shape of the airfoil, some drop in performance vs a conventional airfoil is expected. The area where passengers would sit may cause some aerodynamic problems as the air would have to redirect up the windshield and back down the rear window. Based on the theory described in the previous section, the 2D CFD case should perform better than the 3D case as there will be no finite wing effects in the 2D CFD case. The 3D CFD analysis should agree with the experimental data more than the 2D CFD analysis. The lift curves produced in all tests should have a linear slope up to the point of stall, then drop drastically. The camber in the airfoil should give a nonzero lift at AoA=0.

5. Methodology

5.1. Modelling and Printing

To begin, the airfoil profile was modeled in SolidWorks. As seen in figure 3, the profile was traced using a side view of a 2005 Honda Civic. Two modifications were made to improve the aerodynamics. The wheels were removed to ensure the flow is attached on the entire bottom surface of the airfoil. A sharp trailing edge was added as well to enforce the Kutta condition and ensure no flow traveled from the lower surface to the upper surface at the trailing edge. The resulting profile is shown in figure 14.

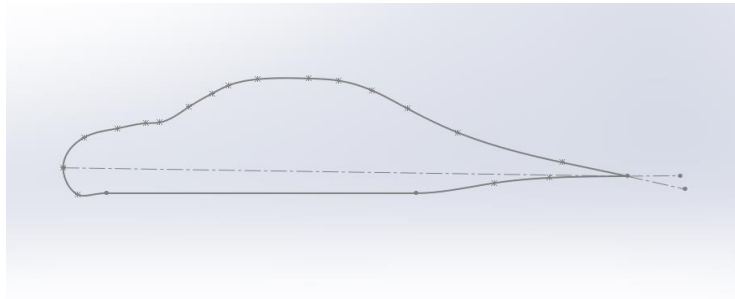


Figure 14: Profile of CVCII wing

At this point, the profile could be converted to a surface and used for the 2D CFD analysis. That process will be explained later in this section. Because high aspect ratio wings are less affected by finite wing effects, the span of the CVCII was chosen to be close to the maximum, at 27cm. As explained in section 3.2, the ideal planform shape to minimize induced drag is an ellipse. The profile was copied and pasted onto the plane of the wing tip and the center and tip chord lengths were adjusted until the wing geometry matched all the constraints outlined in the project description. The chord length in the middle and tip of the wing was set to 68 mm and 19.5 mm respectively. The model of the final wing is shown in figure 15.

The measurements of the full wing are as follows:

- Span: $135\text{mm} \times 2 = 27\text{ cm}$
- Max chord length: $68\text{ mm} = 6.8\text{ cm}$
- Volume: $88047.62\text{ cubic millimeters} = 88.0\text{ cm}^3$
- Planform area: $\text{Span} * \text{Max chord} = 184.41\text{ cm}^2$

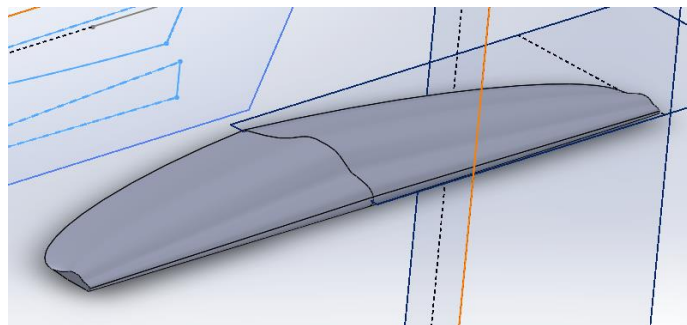


Figure 15: Full wing model of the CVCII in SolidWorks

With the model complete, the wing was printed and assembled. The wing was printed in three parts: the left side, right side, and mount. The three parts were then glued together and sanded down slightly to remove some of the texture from the glue and 3D printing process. The wing was now ready for the wind tunnel test.

5.2. Wind Tunnel Test

The wind tunnel test was performed using the wind tunnel in ENB 010A. The procedure for the wind tunnel test is as follows [7]:

1. Turn on the power supply and allow some time for it to heat up (this reduces the drift in the force transducer)
2. Install the wing into the test section
3. Launch the sensor Java and Arduino applications
4. Open the serial monitor in the Arduino IDE
5. Home the airfoil by entering 'h' through the serial monitor
6. Click log data in the Java application, name and choose the location to save the CSV
7. In the Java application, bias the sensors, and start collecting data immediately after
8. Wait 10 seconds
9. Turn on the wind tunnel
10. Wait 20 seconds or until transients decay
11. Send r through the Arduino serial monitor
12. Wait until sweep is complete
13. Turn off wind tunnel
14. Wait 10 seconds
15. Hit stop collecting

The processing of the experimental data will be shown in section 6.1.

5.3. 2D CFD

The domain was created using Ansys DesignModeler. The profile from figure 14 was used as the airfoil profile for this analysis. A C domain extending 30 chord lengths upstream and 60 chord lengths downstream was used for the domain, which is shown in figure 16. Based on literature [8], the domain size of 60 C downstream would lead to an error in lift coefficient of less than 1%. Ideally, a domain sensitivity study would be done to confirm the error for this specific geometry.

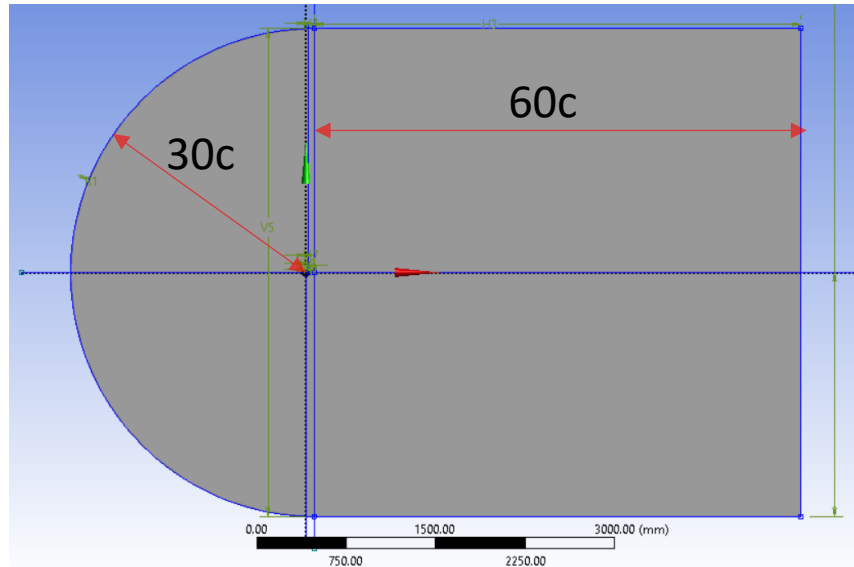


Figure 16: Domain used for 2D CFD analysis

Next, the domain was discretized. The mesh was refined near the wing, and specifically, near the leading and trailing edges. A bias factor was applied to the mesh to increase the cell size further from the geometry.

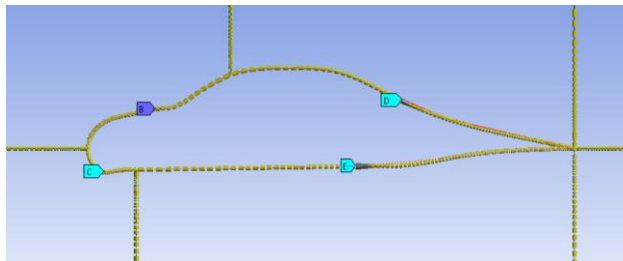


Figure 17: Mesh sizing used for 2D CFD analysis

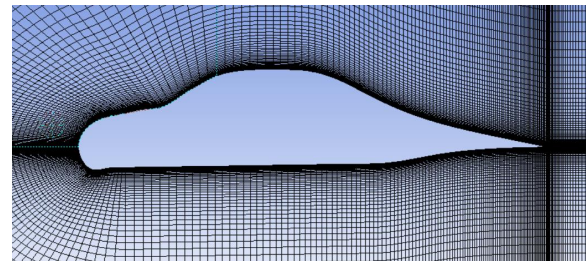


Figure 18: Completed mesh used for 2D CFD analysis

The mesh sizing parameters used at each edge are outlined in table 1 below.

Table 1: Mesh sizing parameters used for coarse mesh for 2D CFD analysis

Sizing zone	Bias factor	Number of cells (Coarse)
Far-field	3000	150
Upper LE	25	90
Upper TE	10	150
Lower LE	20	90
Lower TE	10	180

With the mesh complete, the simulation can be set up. First, the solver settings are chosen. For this analysis, a steady state pressure-based solver is used. The turbulence model is then chosen. For this analysis, the k-omega SST turbulence model is used. It provides a good model for turbulence near walls, as well as in the far-field. The model shows good behavior in separating flows [9].

The air properties are set to match Calgary atmospheric conditions. The atmospheric conditions were recorded during the experimental lab earlier in the year and will be assumed to be similar at the time the wind tunnel test was done. The temperature and pressure readings were 669.6 mmHg and 23.2°C respectively. Using this pressure and temperature, the density is found to be 1.05 kg/m³. The viscosity of air at 23.2°C is 1.83*10⁻⁵ Pa-s [10].

The inlet was set to a velocity inlet, with the velocity being determined by x and y components depending on the AoA. The upper and lower walls of the domain were set to be periodic. The airfoil was set to be a no-slip wall. The outlet was set to an outflow boundary. For the solution methods, the coupled pressure-velocity coupling scheme was used. The SIMPLE scheme led to unstable results and oscillating lift and drag coefficients. The coupled scheme with the pseudo-transient setting on gave good results in terms of solution convergence. As for the discretization schemes, the pressure, momentum, turbulent kinetic energy, and specific dissipation rate were set to second order.

At this point, the calculation can be initialized and run until the residuals do not change. To limit the error due to discretization, a grid convergence study should be done before the main study. The steps outlining the GCS are:

1. Run the simulation, and get output lift and drag coefficients
2. Refine the mesh
3. Repeat steps 1 and 2 until the lift and drag coefficients stop changing between subsequent meshes, or the element limit set by ANSYS Student is met

The main study is carried out with the following steps:

1. Change the x and y velocity of the inlet depending on AoA
2. Change the force vector for lift, drag, and pressure coefficient.
3. Run the simulation
4. Save output lift and drag files
5. Compute inlet area weighted average of pressure, and set as reference value
6. Save pressure coefficient plots
7. Save skin friction coefficient plots
8. Save boundary layer velocity plots
9. Repeat steps 1 through 8 for all AoA from 0 to 20 in increments of 2 degrees

The boundary layer velocity plots are obtained by creating surfaces perpendicular to the upper airfoil surface at a few points along the upper surface and plotting the distance from the wall vs x velocity. The locations of these boundary layer probes are shown in section 6.2.

5.4. 3D CFD

To reduce the number of elements and to keep the area near the wing refined, the domain was reduced significantly in the 3D case. Literature does suggest that the required domain size for a 3D simulation is much smaller than in the 2D case [8], so domain size errors may still be low for this case. The domain used in the 3D CFD analysis is shown in figure 19. The domain extends 15 C upstream and downstream of the wing.

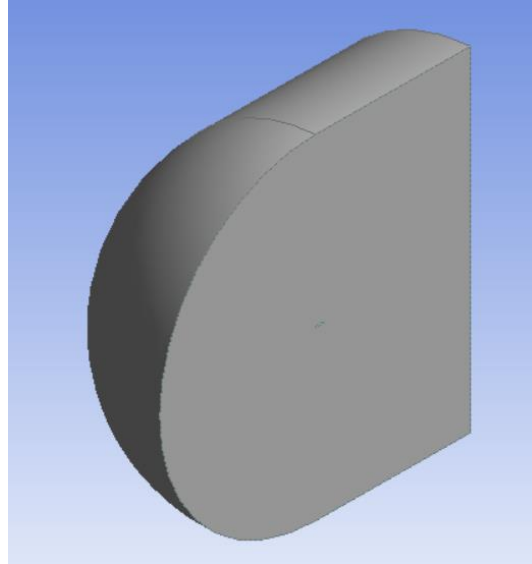


Figure 19: Domain used for 3D CFD analysis

For meshing, face sizing was used on the surface of the wing, and an inflation layer was used to create a zone of structured mesh near the wing. The face sizing on the surface of the wing was set to 1.5mm. The inflation was set to have a maximum of 20 layers. The maximum number of layers, maximum mesh size, and face sizing was modified until a mesh with ~450,000 elements was generated.

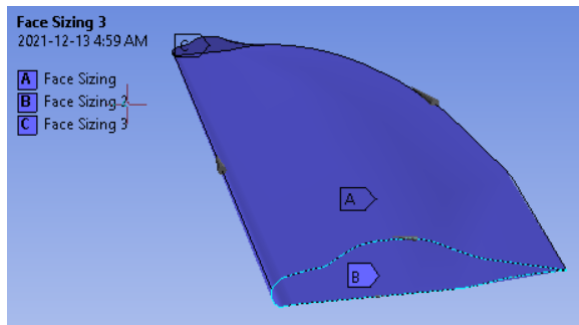


Figure 20: Face sizing selection for meshing for 3D CFD analysis

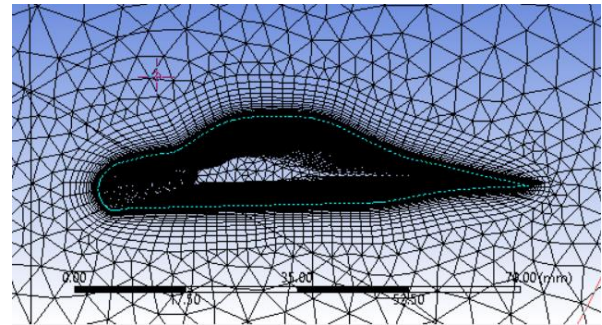


Figure 21: Layer of structured mesh close to airfoil for 3D CFD analysis

With the mesh complete, the simulation set up is very similar to that of the 2D case. The only difference is that the boundary that used to be the top and bottom in the 2D case is set to a velocity inlet in the 3D case.

As with the 2D case, a GCS should be performed on the 3D case. The procedure will be similar, but the mesh refinement will be different. In the 3D case, the number of layers in the inflation layer, the face sizing on the wing, or the maximum element size can be modified to increase or decrease the number of elements in the mesh.

For the main study on the 3D case, the range of AoA is significantly reduced, going from 0 to 16 degrees in increments of 4 degrees.

6. Results and Discussion

6.1. Experimental

The raw data collected during wind tunnel testing was processed so that the important results could be calculated. First, the sensor drift was corrected. For this correction, it is assumed that drift occurs linearly throughout the time that the experiment was run. Data with uncorrected drift is shown in figure 22.

The slope of the drift is found using the equation:

$$m = \frac{d_f - d_i}{\#ofpoints}$$

Where d_f is the final drift calculated by averaging the last 1000 data points and d_i is the initial drift calculated by averaging the first 1000 data points. The denominator is the number of data points collected during the experiment. The data can then be corrected using the equation:

$$data_{corrected} = data - m * n$$

Where n is the number of data points collected since the start of the experiment. An example of the corrected data is shown in figure 23.

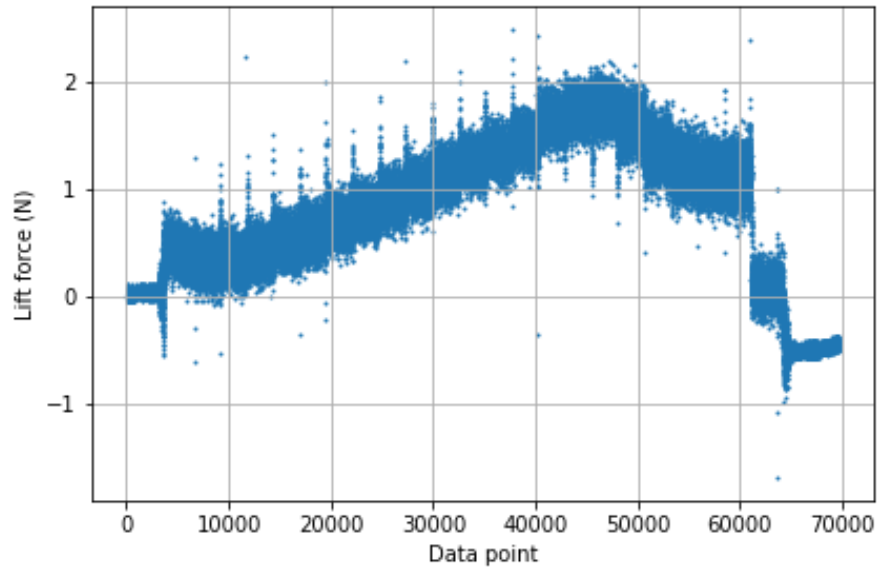


Figure 22: Lift force recorded by force transducer during wind tunnel test

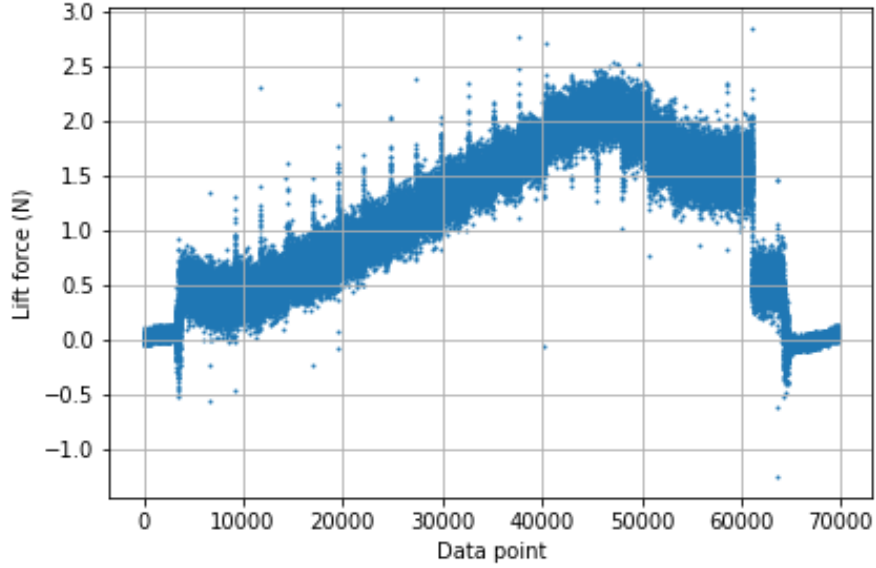


Figure 23: Corrected lift force recorded by force transducer during wind tunnel test

After correcting for drift, the forces and torques at each angle of attack could be determined. Each angle of attack was held for ~20 seconds. The middle ~18 seconds at each angle of attack was used to calculate the average forces and torques. Before the lift and drag coefficients can be calculated, the velocity in the wind tunnel must be corrected to account for blockage. Assuming constant density:

$$A_1 V_1 = A_2 V_2$$

Where A is the cross sectional area of the wind tunnel and V is the velocity. V_2 , the freestream velocity at the wing must be found to calculate the lift, drag, and moment coefficients. The effective area at the wing is approximated as the projection of the wing onto a plane perpendicular to the flow. The area of the projection was determined at an AoA of 0 degrees and 20 degrees. To account for the effect of AoA on the flow area at the wing, the following equation is used:

$$A_{proj} = A_{0^\circ} + \frac{AoA}{20} * (A_{20^\circ} - A_{0^\circ})$$

Where A_{0° is the projected area of the wing at 0 degrees, A_{20° is the projected area of the wing at 20 degrees, and AoA is the angle of attack in degrees. Under the assumption that the projected area increases linearly with angle of attack, this equation provides an approximation of the area blocked by the wing. Now the continuity equation can be used to solve for V_2 :

$$V_2 = A_1 V_1 / A_2$$

Where A_1 and V_1 are the area and velocity of the wind tunnel before the wing, and A_2 is the area at the wing, calculated by subtracting the projected area from the wind tunnel area. With the velocity at the wing known, the dynamic pressure can be calculated for each AoA. With the dynamic pressure at each AoA, the lift and drag coefficients can now be calculated for the wing. Figures 24 to 28 show the lift and drag characteristics of the wing:

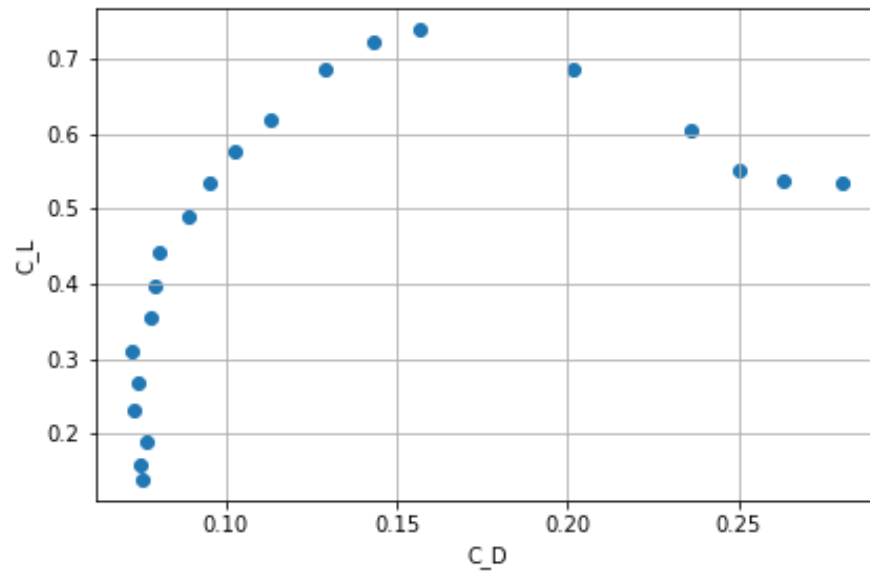


Figure 24: Lift coefficient vs drag coefficient for experimental test

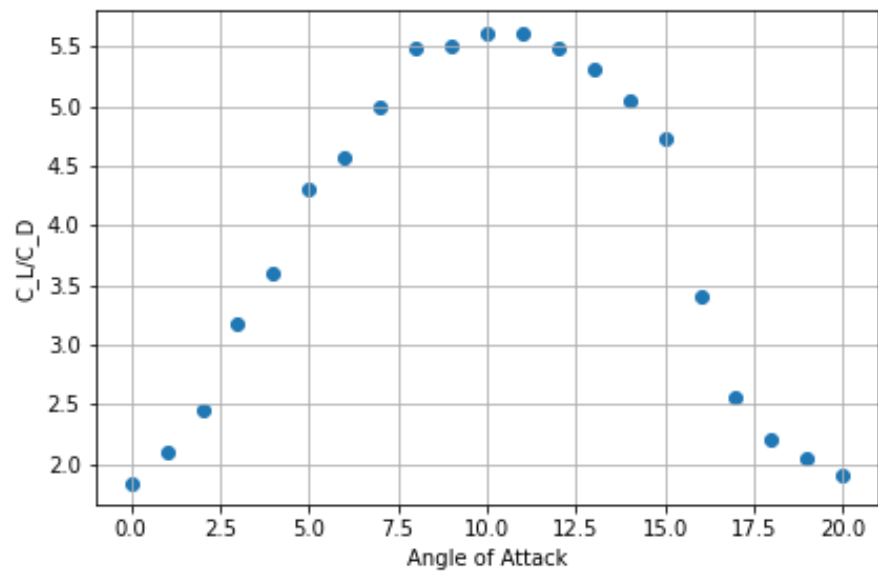


Figure 25: Lift to drag ratio vs angle of attack for experimental test

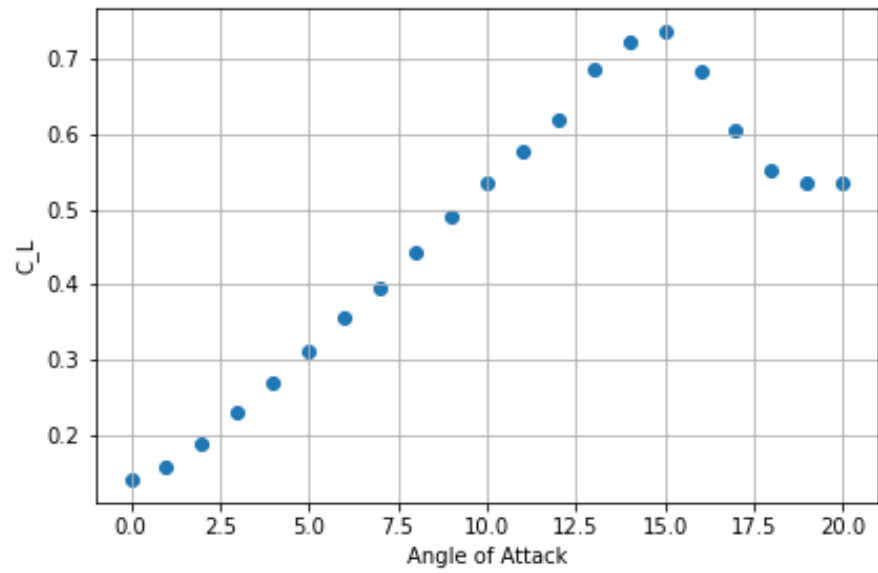


Figure 26: Lift coefficient vs angle of attack for experimental test

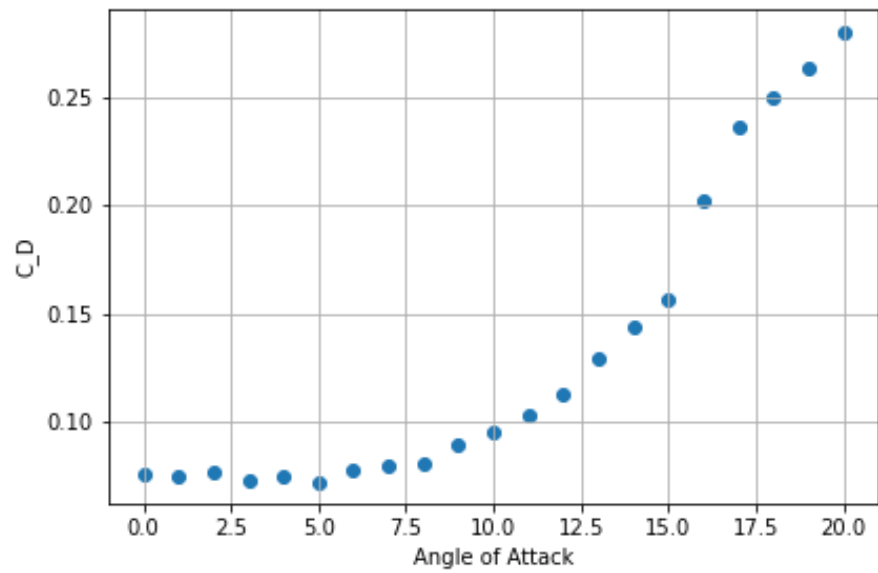


Figure 27: Drag coefficient vs angle of attack for experimental test

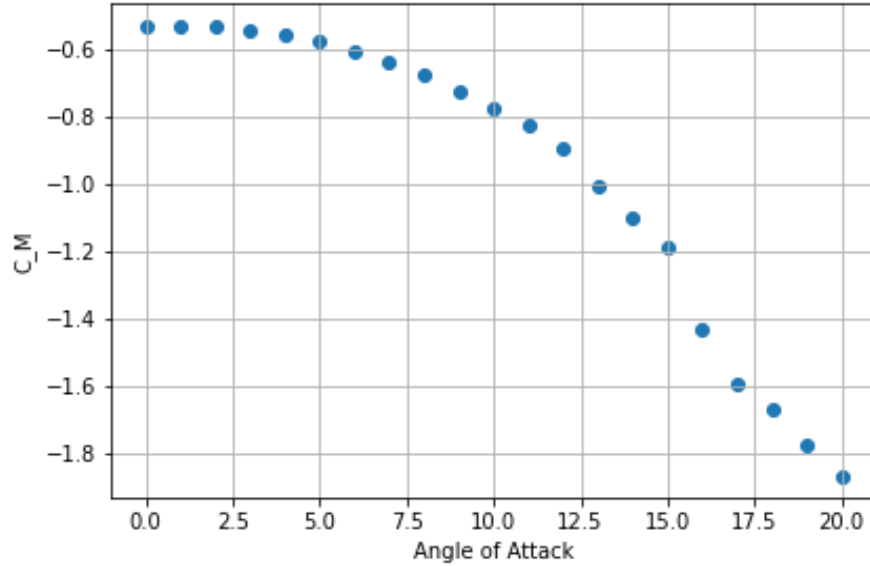


Figure 28: Quarter chord moment coefficient vs angle of attack for experimental test

The aerodynamic center is the point on the wing at which the moment does not change with AoA. For an airfoil or a rectangular wing, this approach is straight-forward, with an analytical solution for the aerodynamic center [1]. With a tapered wing, the analytical solution would be much more difficult to implement. For this wing, the aerodynamic center may be approximated numerically by solving for the moment at several locations along the max chord length at all angles of attack. The moment at any position on the max chord is given by:

$$M_x = M_{c/4} + L \left(x - \frac{c}{4} \right)$$

Where x is the location along the chord from the leading edge to trailing edge and c is the chord length at which the measurements are taken, i.e. the max chord. The moment at several locations along the chord vs AoA is shown in figures 29 and 30.

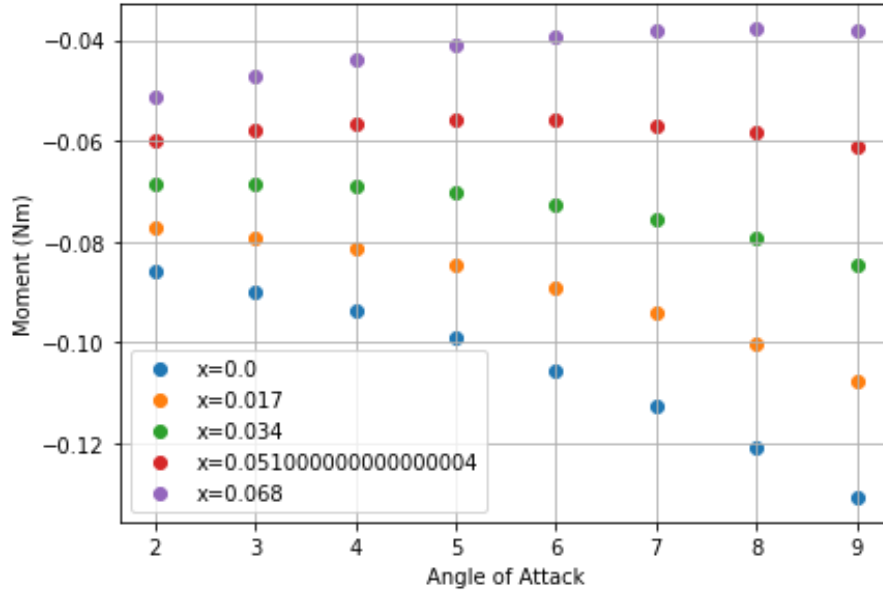


Figure 29: Moment vs angle of attack for several locations along the chord from 0 to 0.068m (Chord length) for experimental test

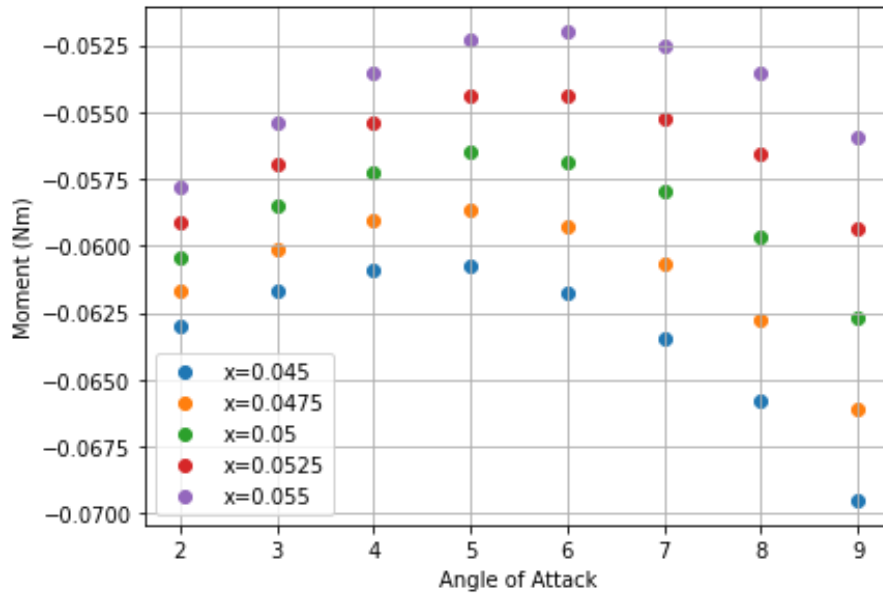


Figure 30: Moment vs angle of attack for several location along the chord from 0.045m to 0.055m for experimental test

The x location along the chord that gives the most constant moment over the range of AoAs is at $x=0.0525\text{m}$, or $x/c=0.772$. Given that aerodynamic centers for cambered wings are typically located near the quarter chord location, this result is questionable. There are several possible reasons for why this value was obtained. The aerodynamic center is typically calculated for airfoils, which would be best approximated using a rectangular wing with a high aspect ratio. Given that the wing used in this experiment is tapered, and other 3D effects such as downwash are present, the aerodynamic center may be affected. Another possible reason is the unconventional wing profile. The protrusion in the

center of the wing may have some effects on the resulting moment that would not be present in a traditional wing.

6.2. Computational Fluid Dynamics – 2D Analysis

Before the main study at a range of angles of attack, a grid convergence study (GCS) was done to minimize the discretization error of the simulation. Five progressively finer meshes were created. The number of elements in each mesh is shown in table 2.

Table 2: Number of elements used for each simulation for grid convergence study in 2D CFD analysis

Mesh	# Elements
Coarser	51000
Coarse	121500
Medium	216000
Fine	337500
Finer	486000

The GCS was performed at an AoA of 6 degrees. The coefficient of lift and drag were used to compare the meshes. The resulting C_l and C_d for the five meshes is shown in figures 31 and 32.

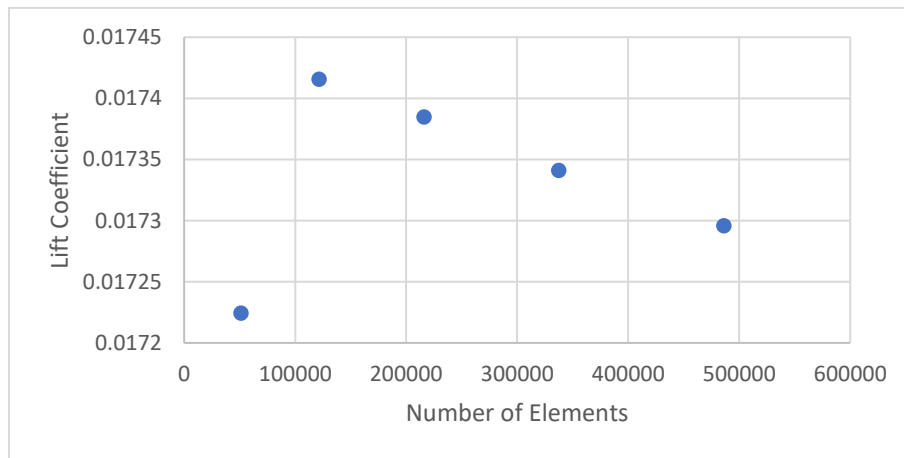


Figure 31: Lift coefficient vs number of elements for AoA=6 in 2D CFD analysis

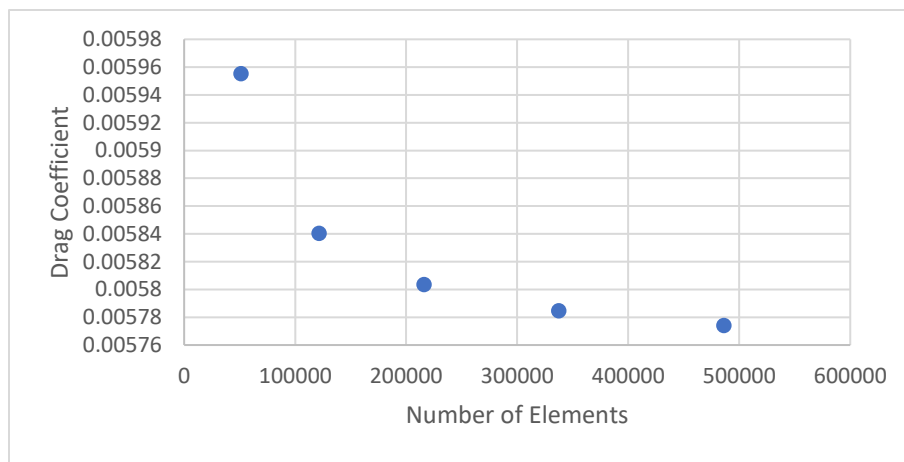


Figure 32: Drag coefficient vs number of elements for AoA=6 in 2D CFD analysis

The drag coefficient appears to approach a converged value; however, the lift coefficient appears to be decreasing even between the fine and finer meshes. Unfortunately, the student version of ANSYS does not allow over 500000 elements for the simulation, so no finer meshes were created. Because the drag coefficient does not appear to change significantly after the fine mesh, the result of the finest mesh will be approximated as the converged drag coefficient. Similarly, the lift coefficient from the finest mesh will be approximated as the converged lift coefficient. Due to the shape of the C_l vs number of cells graph in figure 31, it is likely that there is more error attached with this approximation, however, the exact error cannot be determined due to software restrictions. These approximations will be used to estimate the error in lift and drag coefficient produced by each mesh. The resulting errors are shown in figures 33 and 34.

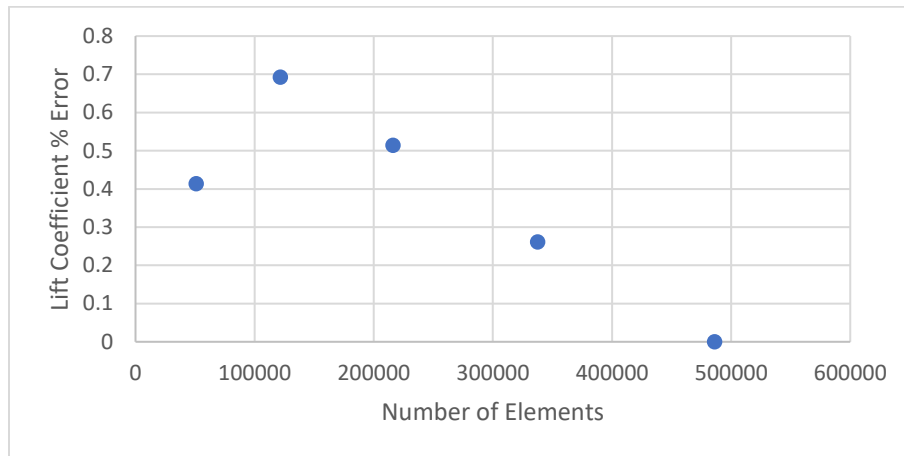


Figure 33: Percent error in lift coefficient vs number of elements for AoA=6 in 2D CFD analysis

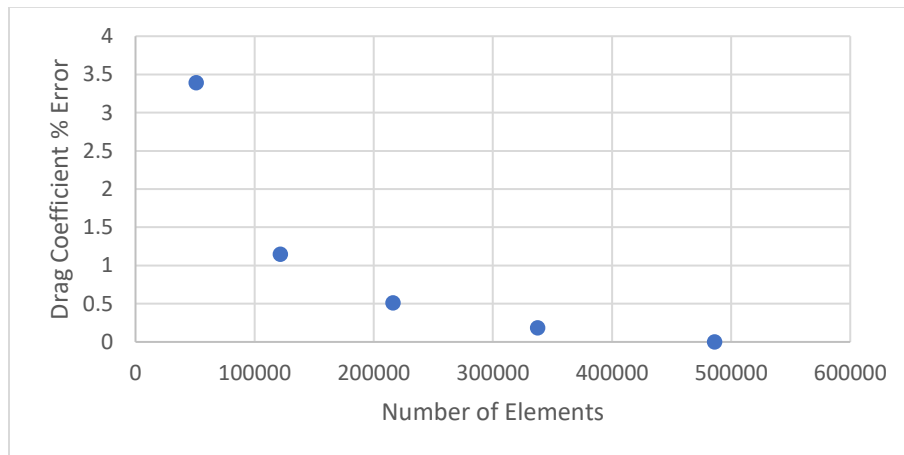


Figure 34: Percent error in drag coefficient vs number of elements for AoA=6 in 2D CFD analysis

For the two-dimensional analysis, the medium mesh will be chosen. With the approximation described previously, the medium mesh gives an error of roughly 0.5% for lift and drag coefficients. The main study was carried out for angles of attack between 0 and 20 degrees in 2-degree increments. Like the experimental section, the lift and drag characteristics from the CFD simulations are shown in figures 35 to 38.

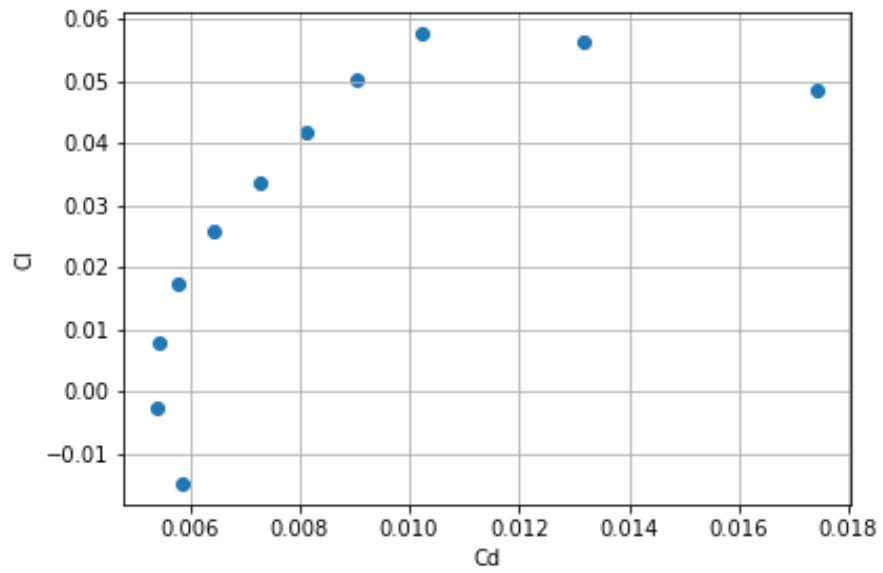


Figure 35: Lift coefficient vs drag coefficient for 2D CFD analysis

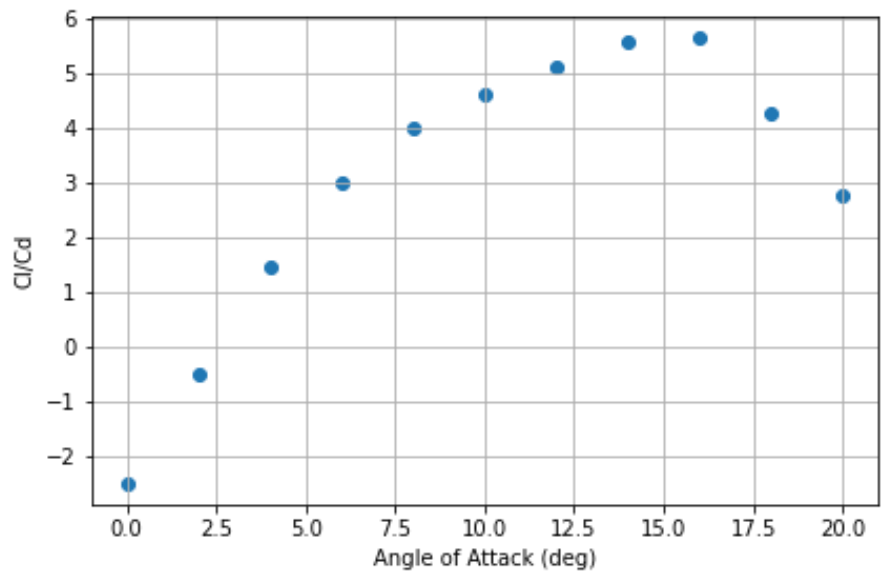


Figure 36: Lift to drag ratio for 2D CFD analysis

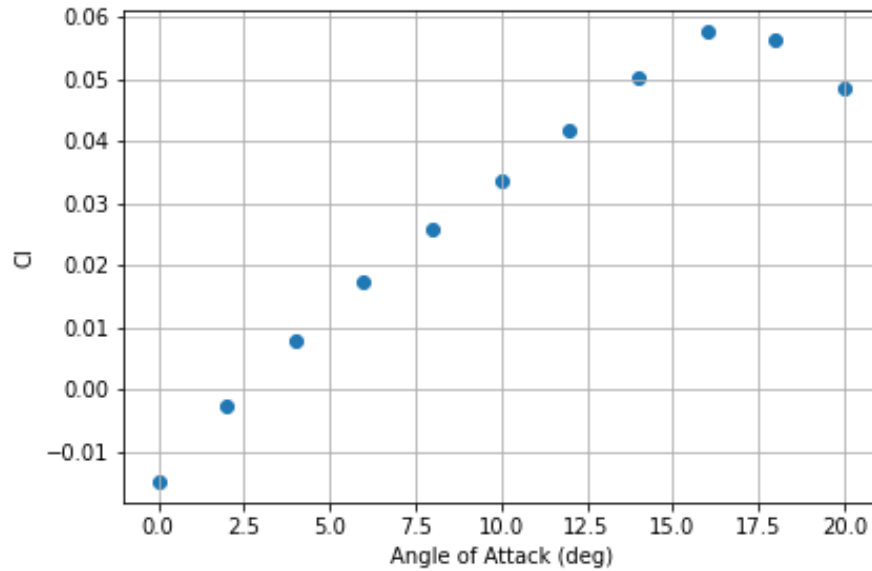


Figure 37: Lift coefficient vs angle of attack for 2D CFD analysis

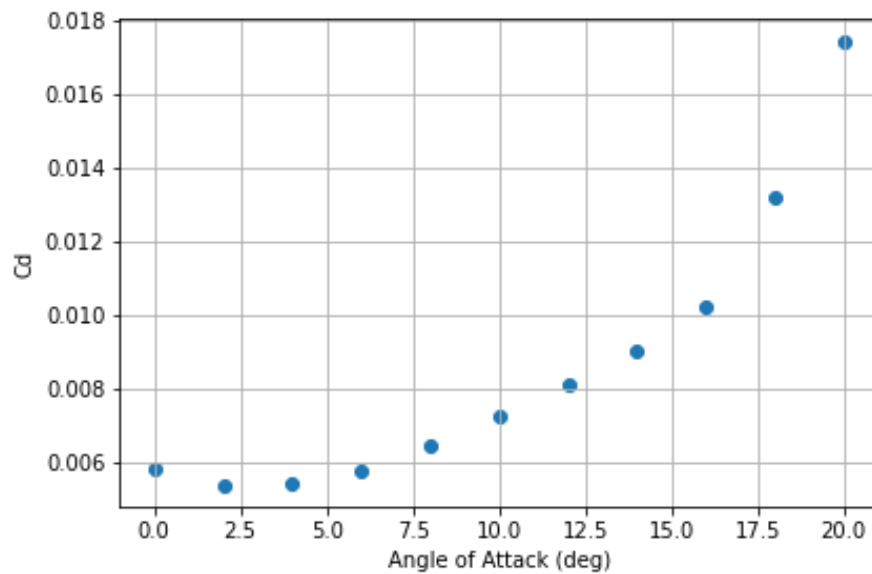


Figure 38: Drag coefficient vs angle of attack for 2D CFD analysis

Additionally, the coefficient of pressure and skin friction coefficient along the airfoil surface was recorded at each AoA. The pre-stall (AoA=10°) and post stall (AoA=20°) pressure coefficients are shown in figures 39 and 40. Likewise, the pre and post stall skin friction coefficients are shown in figures 41 and 42.

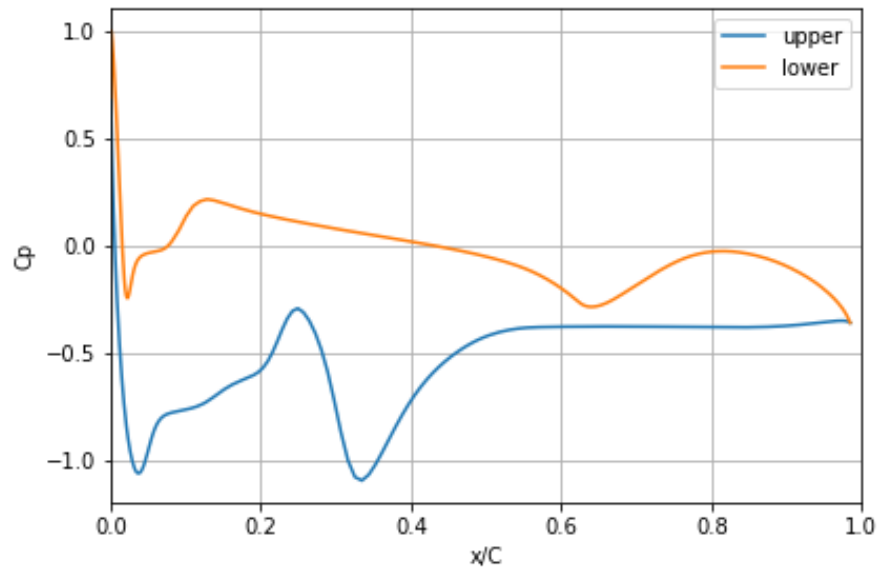


Figure 39: Pressure coefficient on surface of airfoil at AoA=10 for 2D CFD analysis

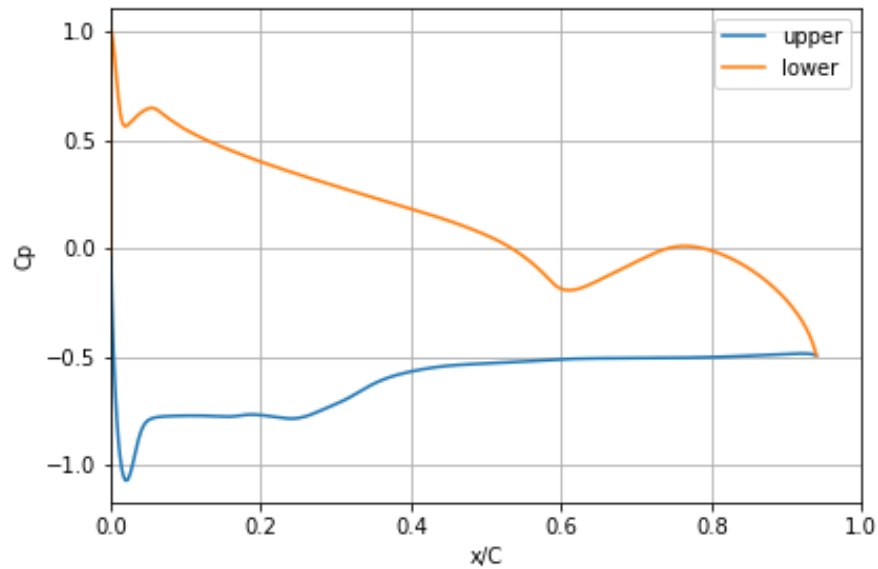


Figure 40: Pressure coefficient on surface of airfoil at AoA=20 for 2D CFD analysis

The effect of two major aspects in the airfoil geometry are evident in figure 39 (AOA=10). In the lower C_p curve, a sharp drop and negative pressure coefficient can be seen near the leading edge. This drop is caused by a small 'bump' on the lower surface of the airfoil. This bump creates a small area of low-pressure recirculating air on the lower surface, which is not ideal for generating lift. This effect will be expanded on later in the report when the 2D CFD is compared to the 3D CFD. Another aspect of the geometry can be seen in the pressure coefficient on the upper surface of the airfoil. The pressure drops initially but has a sharp rise before dropping again at the 0.3C location. This rise and fall is caused by the point in the airfoil where the windshield would be. The pressure increases as the flow redirects around the bottom of the windshield but falls again as the flow expands over the top of the windshield. In the

20-degree AoA case, the flow is separated over the entire upper surface of the airfoil, so the air redirecting is not captured in the pressure coefficient plot. The pressure coefficient contours are shown in figures 43 and 44. The effects described above can be observed in the contour plots. The streamline plots are shown in figures 45 and 46.

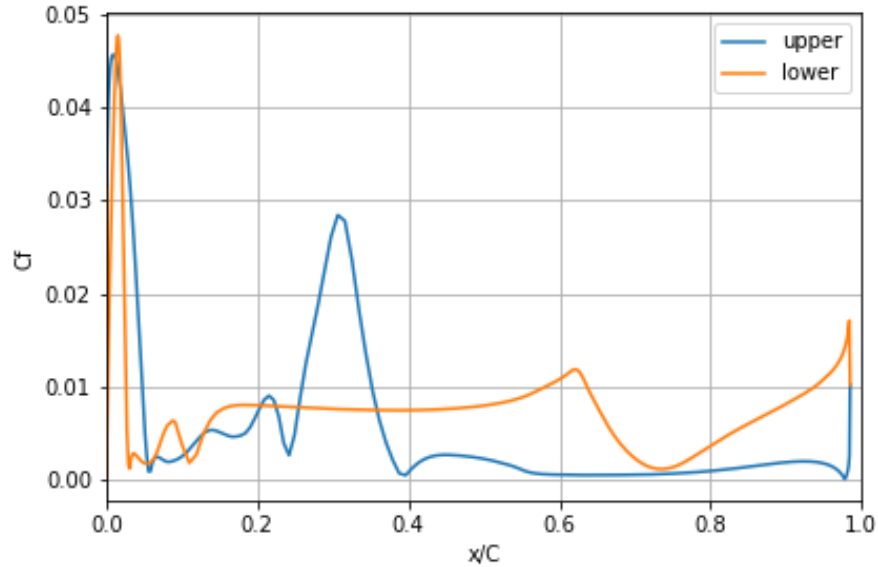


Figure 41: Skin friction coefficient on surface of airfoil at AoA=10 for 2D CFD analysis

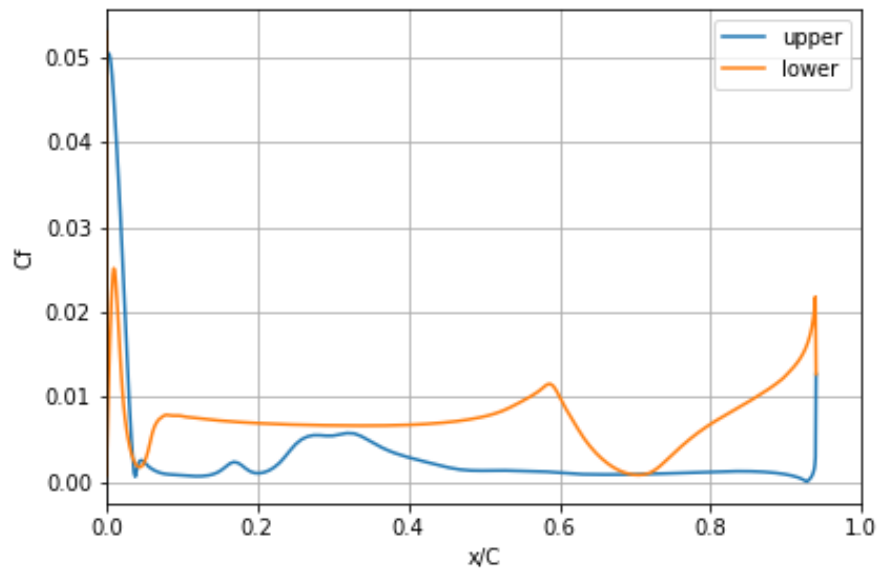


Figure 42: Skin friction coefficient on surface of airfoil at AoA=20 for 2D CFD analysis

As in the pressure coefficient plots, the redirecting flow is captured in the friction coefficient plots as well. At the 0.3C position at AoA=10, the redirecting flow causes a spike in the friction coefficient. The skin friction on the lower surface is similar in both cases, with a drop occurring at the 0.6C location as the airfoil tapers to the trailing edge. One difference, however, is the behavior in the friction coefficient

near the leading edge, at around 0.1C. In the $AoA=10$ case, the bump on the lower surface leads to a wavy friction coefficient as the bump causes the flow to recirculate.

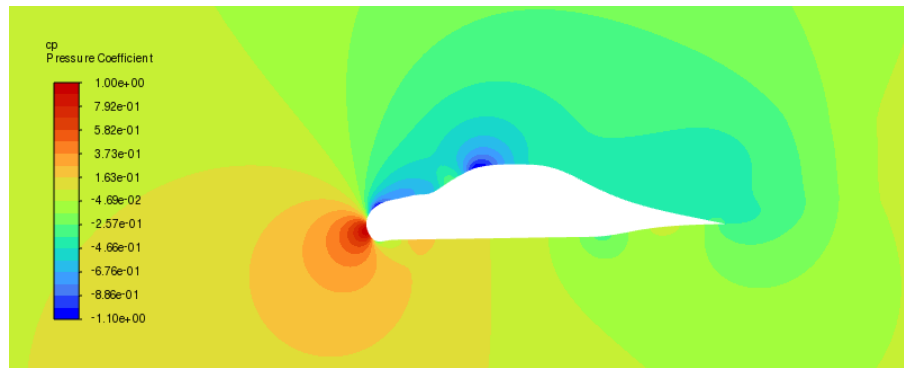


Figure 43: Pressure coefficient contour near airfoil at $AoA=10$ for 2D CFD analysis

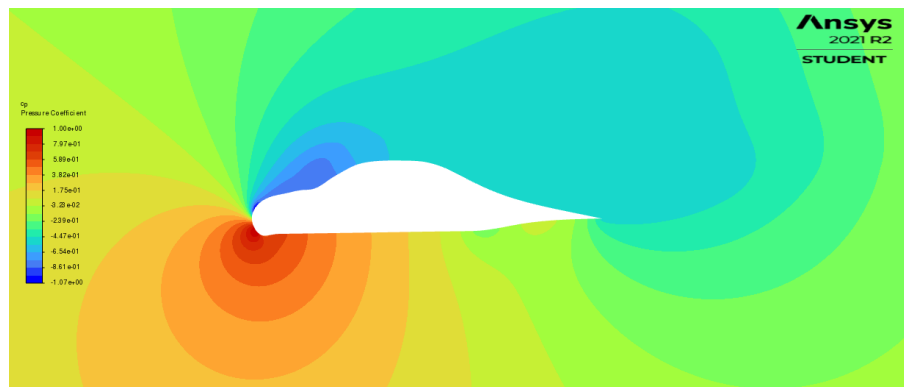


Figure 44: Pressure coefficient contour near airfoil at $AoA=20$ for 2D CFD analysis

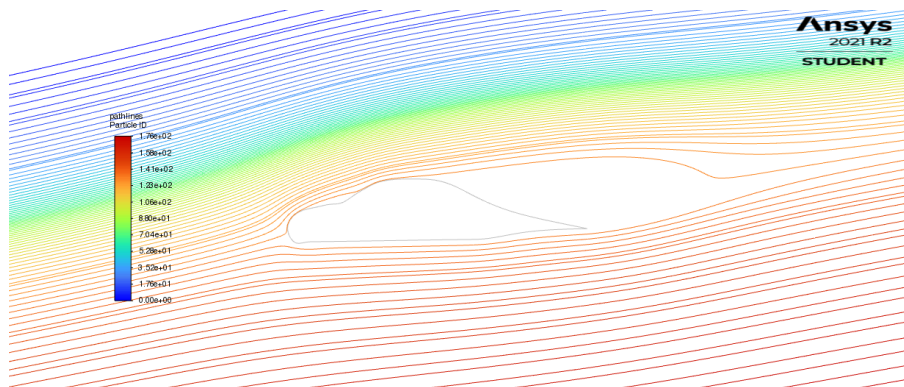


Figure 45: Streamlines near airfoil at $AoA=10$ for 2D CFD analysis

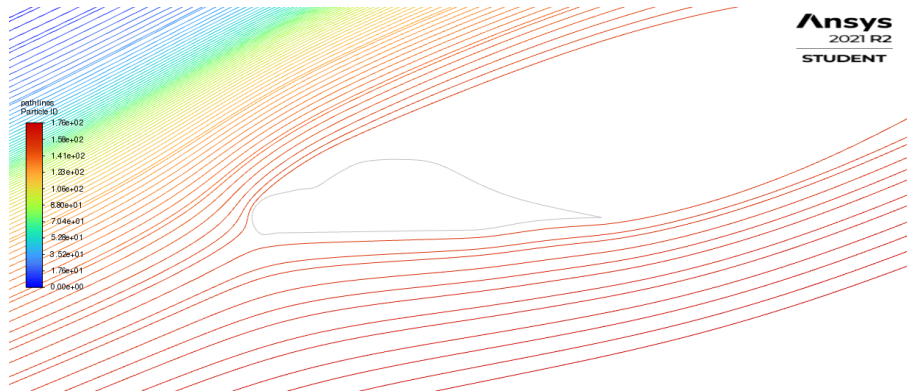


Figure 46: Streamlines near airfoil at AoA=20 for 2D CFD analysis

The streamlines give more insight into how the airfoil performs. In the AoA=10 case, the streamlines on the top surface stay attached up to the point at which the passengers would be sitting (0.55C). The flow after this point is separated. Unfortunately, this behavior occurs even at low angles of attack. The streamlines in the AoA=20 case shows the flow separating off the leading edge, meaning the wing is at a full stall at this point. These effects are further illustrated in the boundary layer visualizations at three points along the top surface of the airfoil. The black lines in figure 47 show the locations at which the boundary layer velocity is recorded.

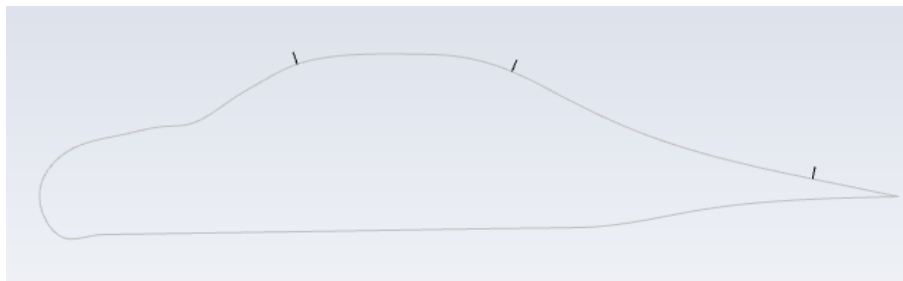


Figure 47: Location of boundary layer probes on airfoil surface for 2D CFD analysis

Once again, the AoA=10 and AoA=20 cases are used for comparison, the boundary layer visualizations are shown in figures 48 and 49.

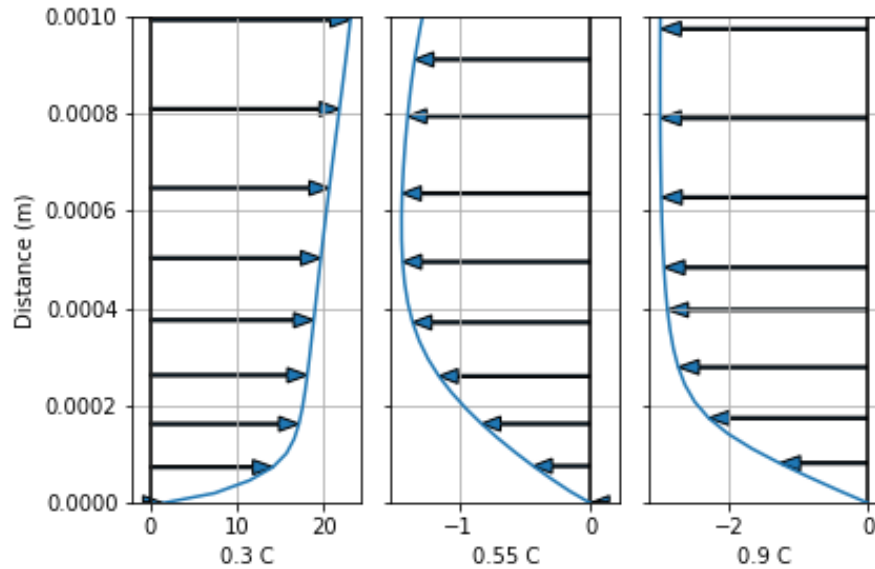


Figure 48: Distance away from airfoil surface vs velocity at three locations along upper surface of airfoil at AoA=10 for 2D CFD analysis

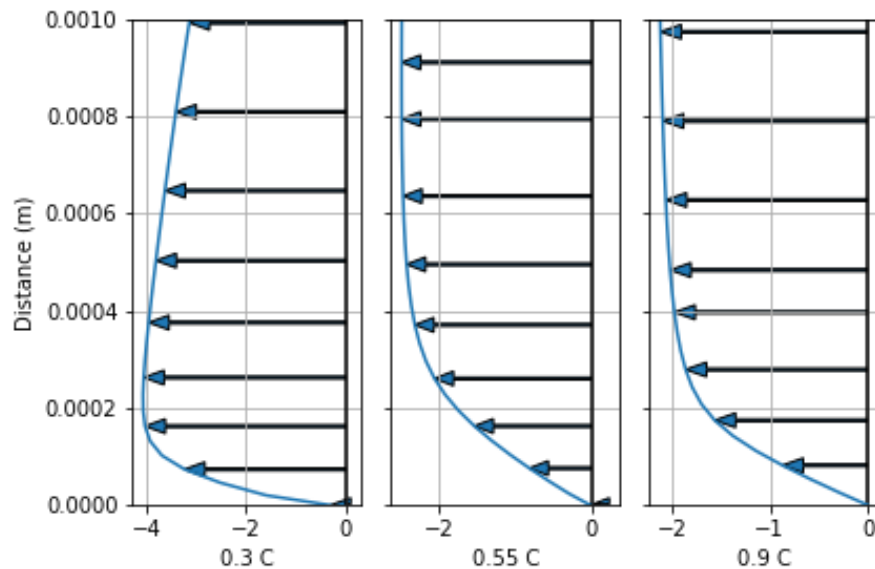


Figure 49: Distance away from airfoil surface vs velocity at three locations along upper surface of airfoil at AoA=20 for 2D CFD analysis

For the AoA=10 case, the flow is still attached at the 0.3C location, at the top of the windshield. At 0.55C, the flow is already separated. This effect was seen in the streamlines for this case as well. For the AoA=20 case, the flow is separated from the leading edge, therefore the flow is recirculating at all three locations. Once again, this is supported by the streamlines plot.

6.3. Computational Fluid Dynamics – 3D

Like with the two-dimensional case, a GCS was performed on the three-dimensional case at an angle of attack of 4 degrees. The lift and drag coefficients vs number of elements is shown in figures 50 and 51.

The lift and drag coefficients change drastically as the mesh is refined. There is a 7.4% change in lift coefficient between the finer and finest meshes for the 3D grid convergence study. As a comparison, there is a 0.26% change in lift coefficient in the finer and finest meshes used for the 2D CFD grid convergence study.

Table 3: Number of elements used for each simulation for grid convergence study in 3D CFD analysis

Mesh	# Elements
Medium	300606
Finer	365589
Finest	435586

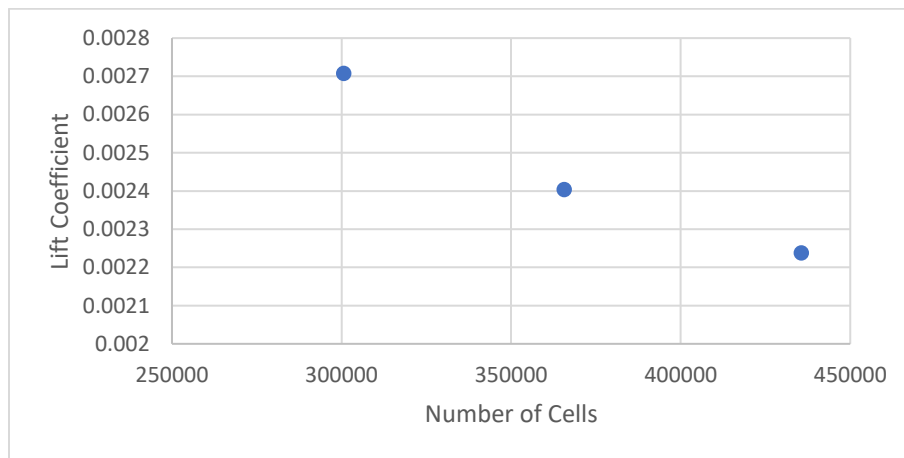


Figure 50: Lift coefficient vs number of elements in grid convergence study for 3D CFD analysis

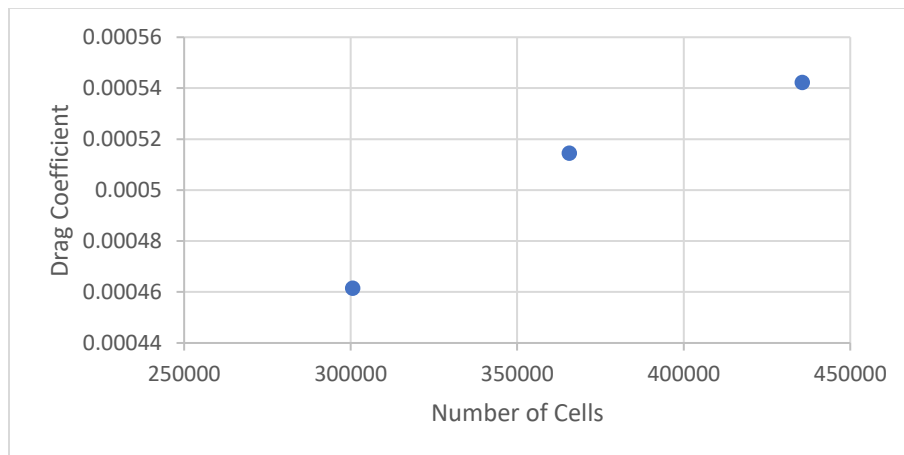


Figure 51: Drag coefficient vs number of elements in grid convergence study for 3D CFD analysis

Further mesh refinements would be required for a more conclusive GCS on the 3D case. Unfortunately, even with a significantly reduced domain size and significantly larger element size, the number of elements quickly approached the maximum allowed by ANSYS Student. For the remainder of the 3D analysis, the finest mesh will be used, although, based on the results of the GCS, the results may be

inaccurate. Nevertheless, the 3D case will be valuable in analyzing finite wing effects that are not seen in the 2D case. The lift and drag characteristics from the 3D CFD are shown in figures 52 and 53.

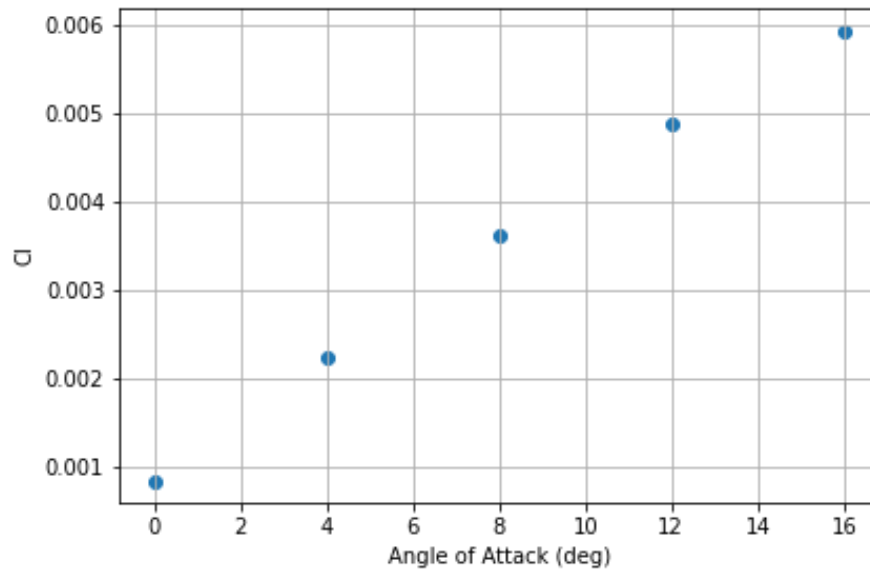


Figure 52: Lift coefficient vs angle of attack for 3D CFD analysis

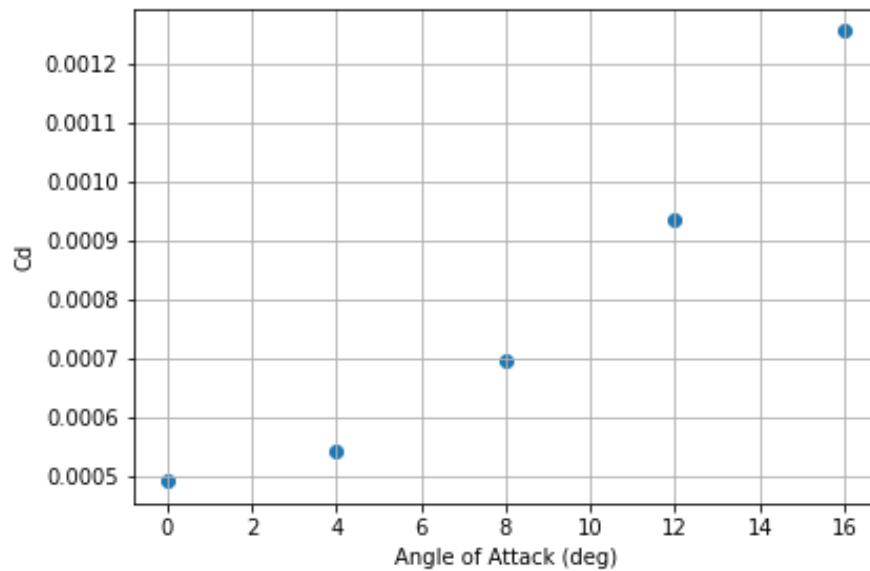


Figure 53: Drag coefficient vs angle of attack for 3D CFD analysis

Additionally, the pressure coefficient was recorded for all angles of attack at three spanwise locations; 0mm, 50mm, and 100mm. The pressure coefficient plots for AoA of 8 degrees and 16 degrees are shown in figures 54 and 55.

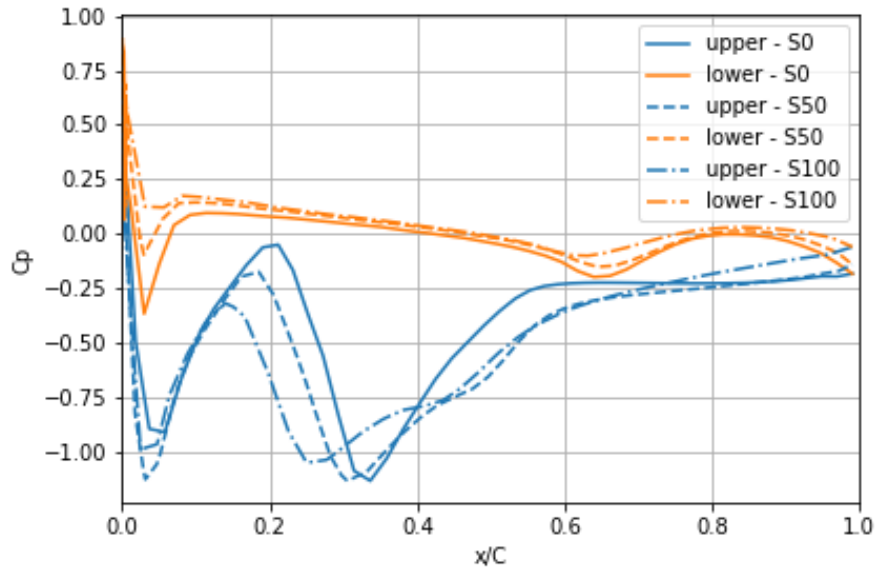


Figure 54: Pressure coefficient at three spanwise locations along surface of wing at $AoA=8$ for 3D CFD analysis

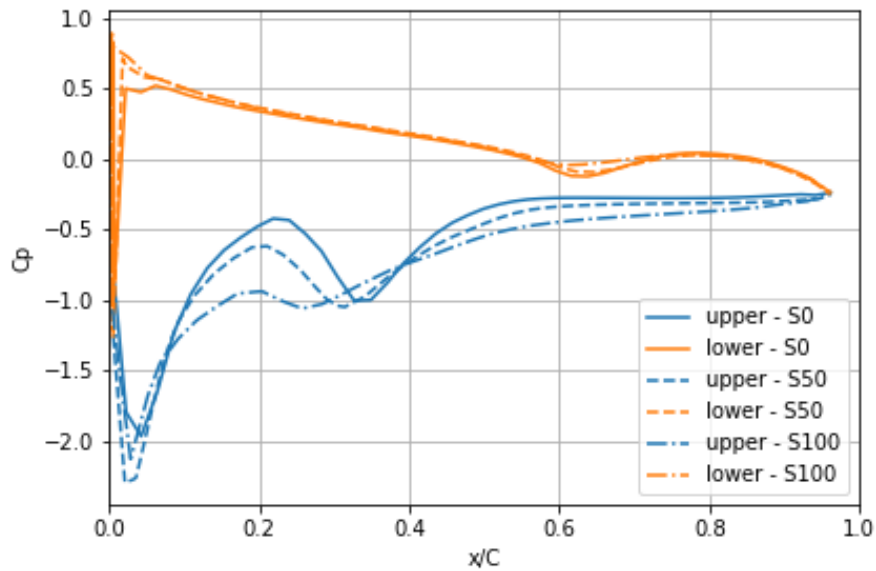


Figure 55: Pressure coefficient at three spanwise locations along surface of wing at $AoA=16$ for 3D CFD analysis

The pressure coefficient on the lower surface of the wing is mostly constant throughout, but the pressure coefficient profile on the upper surface changes based on spanwise location. As seen in the 2D case, there is a pressure increase at the $0.2C$ location, which corresponds roughly to the start of the windshield. This effect has less prominence as the spanwise location approaches the tips. This is likely due to the profile of the wing getting smaller from the middle to the tip, resulting in the windshield area of the profile having less effect on the flow. Streamlines were used to visualize the flow pattern near the top and bottom surfaces, and the tip of the wing. Streamlines for an AoA of 0° and 16° are shown in figures 56 to 59.

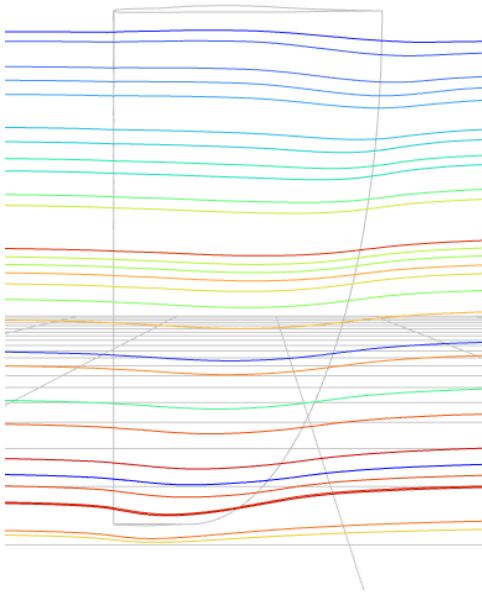


Figure 56: Streamlines above wing at $AoA=0$ for 3D CFD analysis

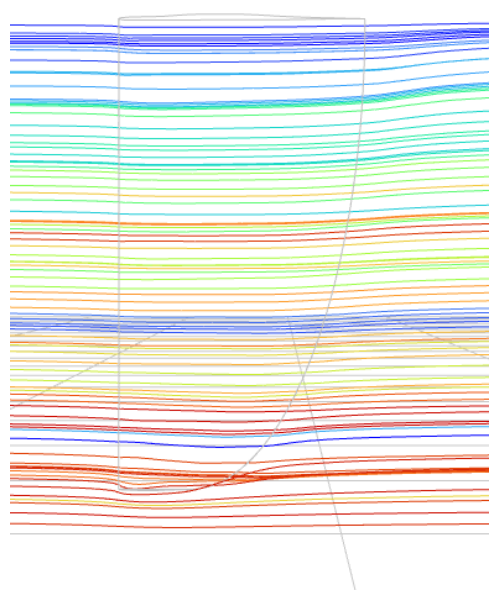


Figure 57: Streamlines below wing at $AoA=0$ for 3D CFD analysis

As seen in figure 57, small tip vortices are beginning to form. However, these do not appear to have a major effect on the rest of the streamlines. The effect of the tip vortices becomes more prominent at a higher angle of attack when more lift is generated, as seen in figures 58 and 59.

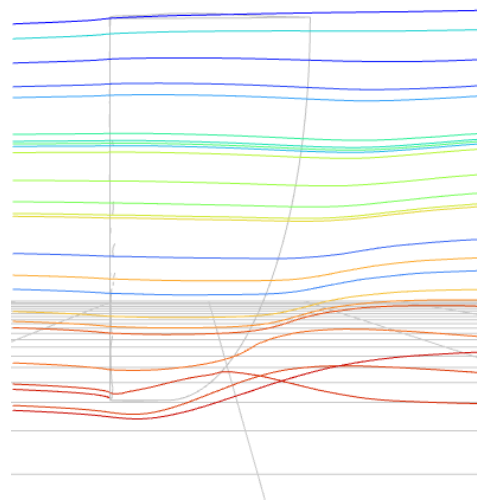


Figure 58: Streamlines above wing at $AoA=16$ for 3D CFD analysis

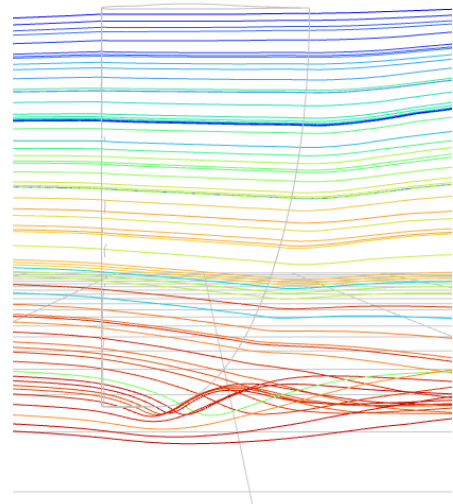


Figure 59: Streamlines below wing at $AoA=16$ for 3D CFD analysis

The intensity of the tip vortices is increased as the AoA is increased. The vortices also appear to be affecting the flow over the wing, as the streamlines on the top surface are turned slightly towards the middle of the wing and the streamlines on the bottom surface are turned slightly towards the tip.

6.4. Comparison of Results

Before comparing the lift and drag coefficients of the three tests, the lift and drag must be converted an area-based lift and drag. Reference values were not set in ANSYS, so conversions were done after the results were obtained. For the sectional lift coefficient in the 2D case, the conversion is:

$$C_L = c_{l_{ANSYS}} * span/A$$

Where span is the span of the actual wing and A is the area of the wing. A similar conversion was done for the 3D case:

$$C_L = c_{l_{ANSYS}} * 2/A$$

The factor of 2 was added because only half the wing was simulated in the 3D CFD section. The equations are the same for lift and drag coefficients. With the lift and drag coefficients converted to the same form, they can now be compared. The comparison is shown in figures 60 and 61.

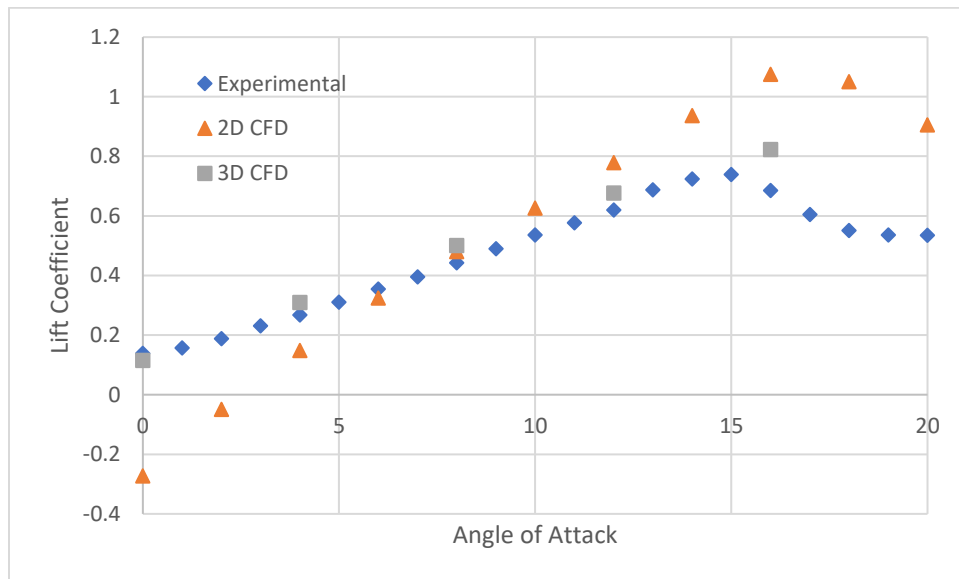


Figure 60: Lift coefficient vs angle of attack for all three tests

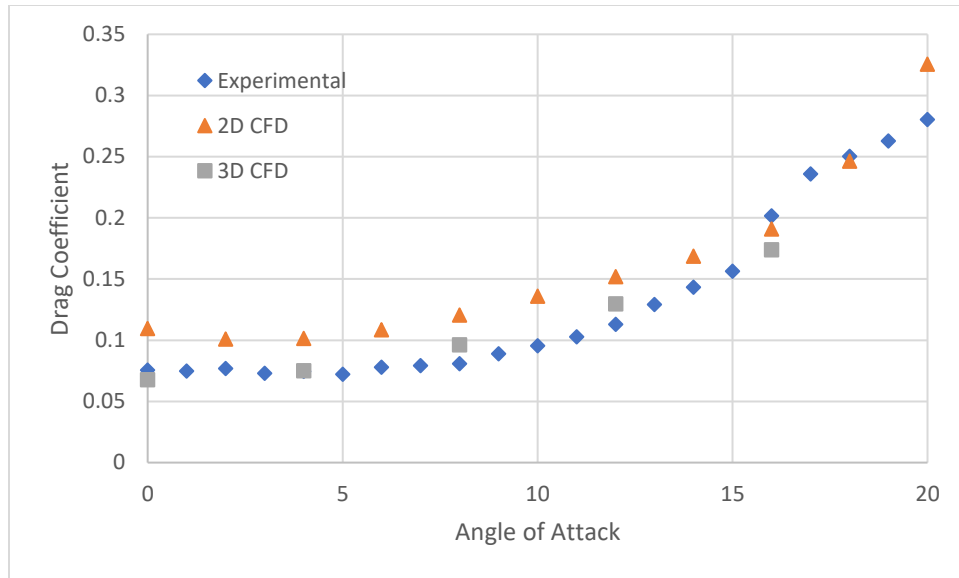


Figure 61: Drag coefficient vs angle of attack for all three tests

The results of the 3D CFD match the experimental results much better than the 2D CFD. Two differences in the lift curves between the 2D and 3D cases are the slope of the pre-stall lift and the lift at AoA=0. The slope of the lift angle in the 2D case is much higher than in the 3D case. This is most likely due to finite wing effects. Specifically, tip vortices leading to downwash will lower the effective angle of attack. This effect is stronger as the lift is increased, leading to the lower lift curve slope in the 3D cases. The lift slope is calculated as an average slope between AoA=4 and AoA=12 for all tests. The lift slopes are shown in table 4.

Table 4: Slope of lift curve for all three tests done on CVCII

Test	Slope of lift curve
Experimental	2.597 rads ⁻¹
2D CFD	4.739 rads ⁻¹
3D CFD	2.682 rads ⁻¹

The lift slopes for all tests deviate significantly from the theoretical lift curve slope of 2π as discussed in section 3.1. The 2D CFD case likely deviates from the theoretical lift curve slope due to the unconventional shape not behaving like a thin airfoil.

The 0-degree AoA lift is also different between the 2D and 3D cases. The reasoning for this becomes evident when looking at the pressure coefficient contours for the 2D and 3D cases at AoA=0. The pressure coefficients are shown in figures 62 and 63.

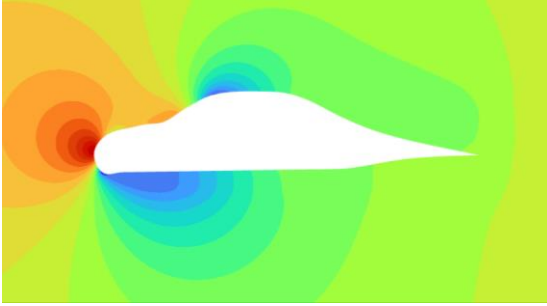


Figure 62: Pressure coefficient contour at AoA=0 for 2D CFD analysis

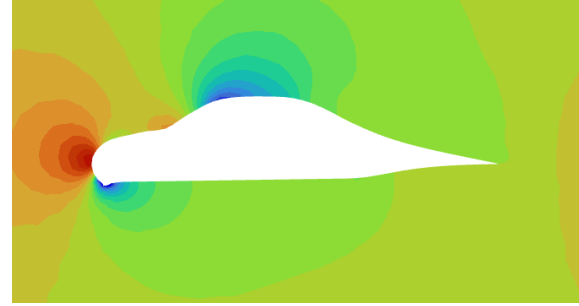


Figure 63: Pressure coefficient contour at AoA=0 for 3D CFD analysis

The pressure coefficient contours appear similar on the upper surface of the airfoil; however, the area of interest is the lower surface. In the 2D case, the lower surface bump creates a low-pressure zone that propagates to around the 0.5C location. This effect is not captured in the 3D case. The bump still creates a low-pressure zone, but the pressure recovers much faster than in the 2D case. The pressure coefficient plots on the airfoil/wing surface shown in figures 64 and 65 further illustrates this effect.

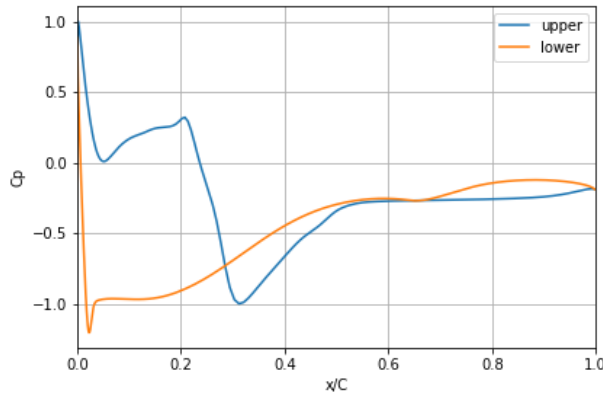


Figure 64: Pressure coefficient along surface of airfoil at AoA=0 for 2D CFD analysis

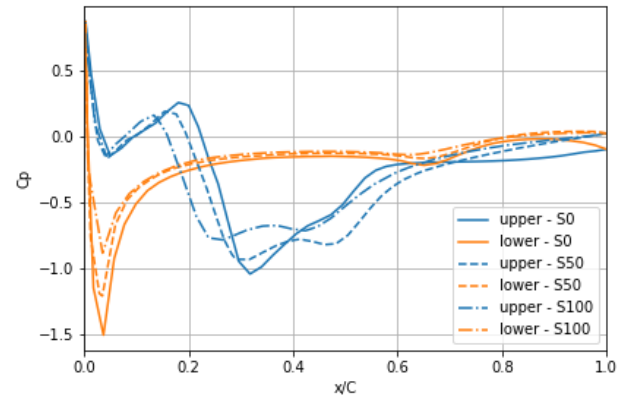


Figure 65: Pressure coefficient along surface of wing at three spanwise locations at AoA=0 for 3D CFD analysis

As described above, the pressure on the lower surface recovers much faster in the 3D case than in the 2D case. Initially, this effect was thought to be caused by the coarse mesh in the 3D case not capturing the recirculation causing the low-pressure zone. However, the results of the 3D case match closely with experimental results, meaning it is likely that the 3D case can still be viewed as a representation of what is happening in the real world. The exact mechanism of the pressure recovery is unknown; however, some speculation can be made. Perhaps the 2D case is more constrained in how high- and low-pressure zones are formed, resulting in the large low pressure zone being part of the stable solution in the 2D case.

The lift coefficient vs drag coefficient and lift to drag ratio vs AoA for all three tests are shown in figures 66 and 67.

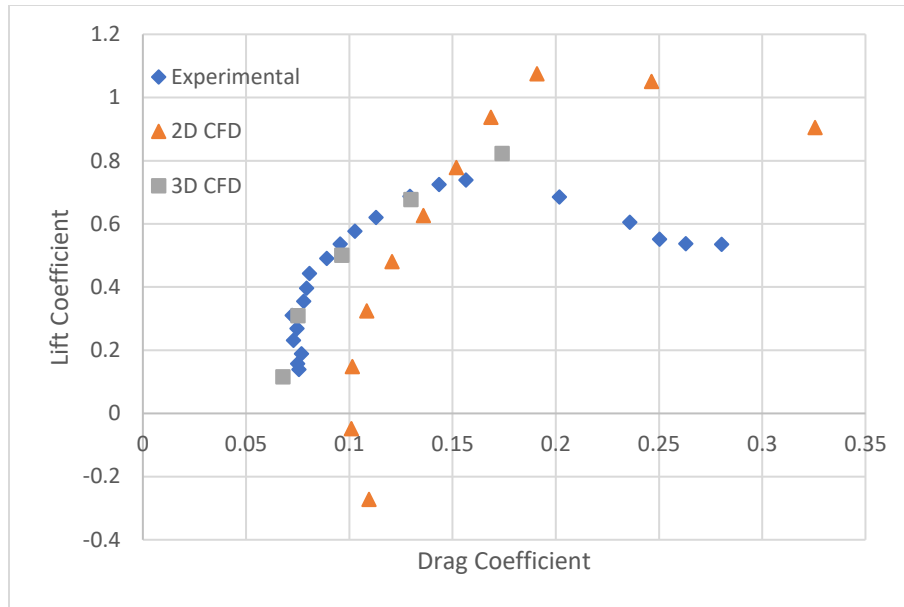


Figure 66: Lift coefficient vs drag coefficient for all tests on CVCII

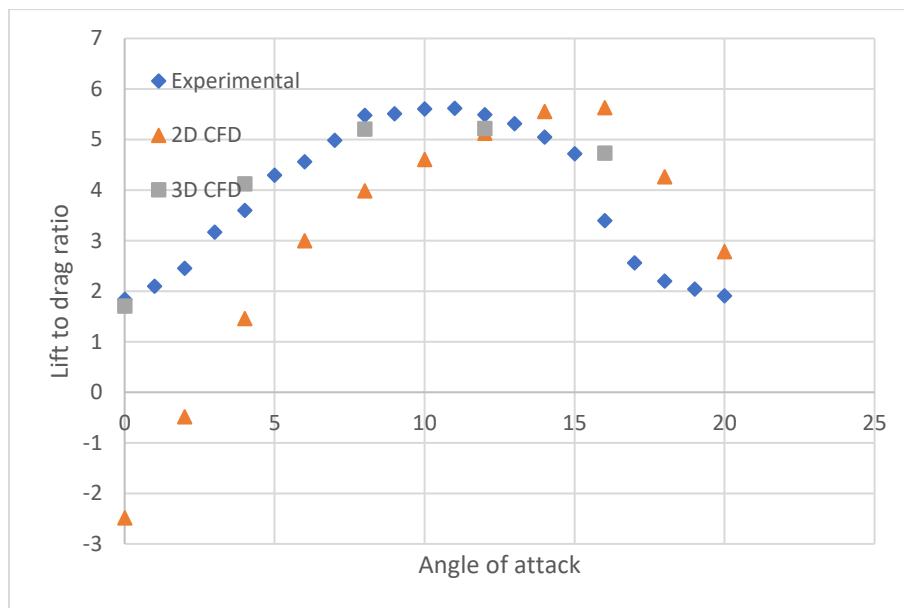


Figure 67: Lift to drag ratio vs angle of attack for all tests on CVCII

Like with the lift and drag vs angle of attack, the 3D CFD and experimental results in the above two figures show good agreement, with the 2D results deviating from both. The maximum lift to drag ratio and lift at stall along with their respective angles of attack are summarized in table 5.

Table 5: Maximum lift to drag ratio and lift to stall with respective angles of attack for all tests done on the CVCII

Test	Max C_l/C_d	AoA at Max C_l/C_d	C_l at stall	AoA at stall
Experimental	5.618	11	0.739	15
2D CFD	5.634	16	1.075	16
3D CFD	5.220	12	0.8032	16

6.5. Comparison with existing airfoil designs

Because the wing used in this project is a new design, there are no existing literature values for comparison. Instead, the lift and drag characteristics will be compared against two select NACA airfoils. The NACA 2415 and NACA 23024 are used for comparison. These two airfoils were chosen because their thick shape somewhat resembles the CVCII profile. The two airfoils are shown in figures 68 and 69.

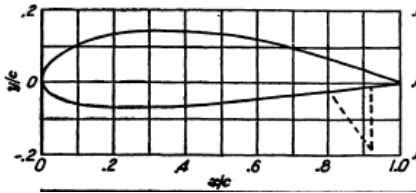


Figure 68: NACA 2415 airfoil profile [11]

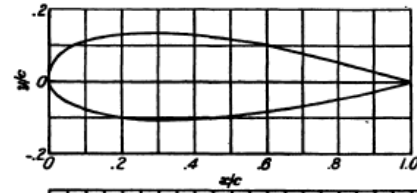


Figure 69: NACA 23024 airfoil profile [11]

The lift and drag coefficient of the two NACA airfoils are compared with the CVCII in figures 70 and 71. The Reynolds number at which the data is taken can be determined using the test conditions:

$$Re = \frac{\rho V D}{\mu}$$

Where ρ is the density, V is the freestream velocity, D is the characteristic length (the chord length in this case), and μ is the viscosity of air.

$$Re = \frac{1.05 \text{ kg/m}^3 * 18.2 \text{ m/s} * 0.068 \text{ m}}{1.83 * 10^{-5} \text{ Pa-s}} \approx 71000$$

The 2D CFD case has a max lift coefficient on the same order as the two NACA airfoils, with a max C_L of 1.075, while the NACA 2415 and NACA 23024 have a max C_L of ~ 1.1 and ~ 0.91 respectively. There are drastic differences in the drag characteristics of the CVCII when compared to the more conventional NACA airfoils, specifically with the NACA 2415, with the drag coefficient being consistently $\sim 3x$ larger for the CVCII. This behavior is likely due to the flow separation characteristics of the CVCII. Even at low angles of attack, the streamlines do not follow the top surface of the airfoil to the trailing edge and instead, separate at the $\sim 0.55c$ location. This separation leads to an increase in pressure drag that would not be present in the NACA 2415 until the point of stall.

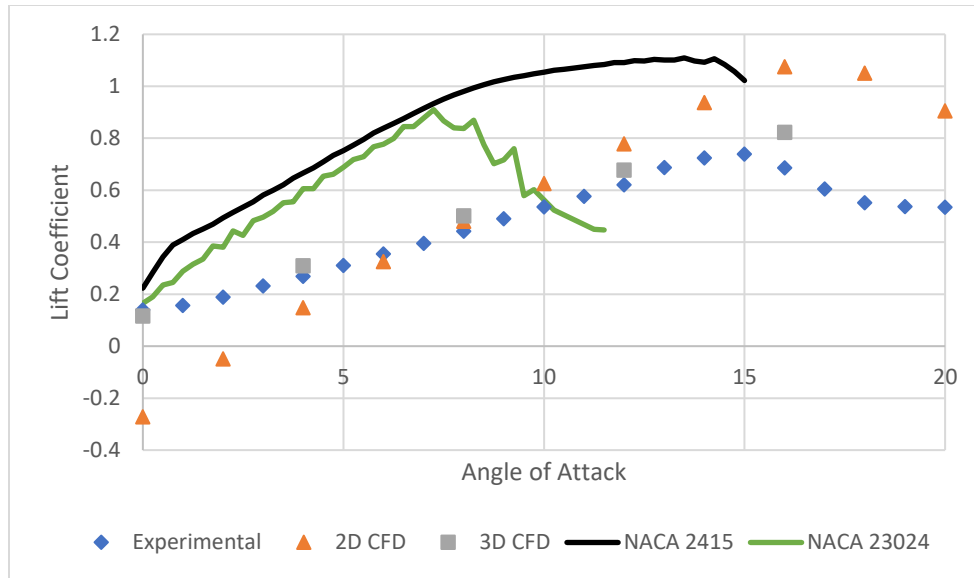


Figure 70: Lift coefficient vs angle of attack for all tests on CVCII and experimental data on select NACA airfoils [3]

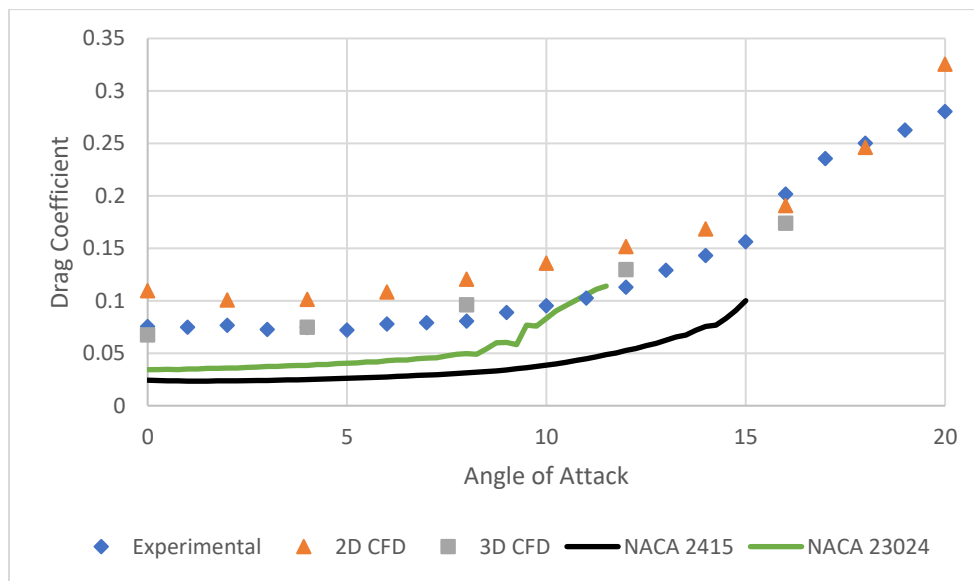


Figure 71: Drag coefficient vs angle of attack for all tests on CVCII and experimental data on select NACA airfoils [3]

When comparing the lift to drag ratio, the NACA airfoils perform drastically better, with the maximum lift to drag ratio being on the order of 20 to 30. For the CVCII, the maximum lift to drag is 5.63 (2D CFD case). Although the maximum lift to drag ratio is much lower, the lift to drag ratio has a shallower drop off after stall. The lift to drag ratio vs angle of attack for the CVCII is compared with the NACA airfoils in figure 72 and emphasizes why wings should not be shaped like cars.

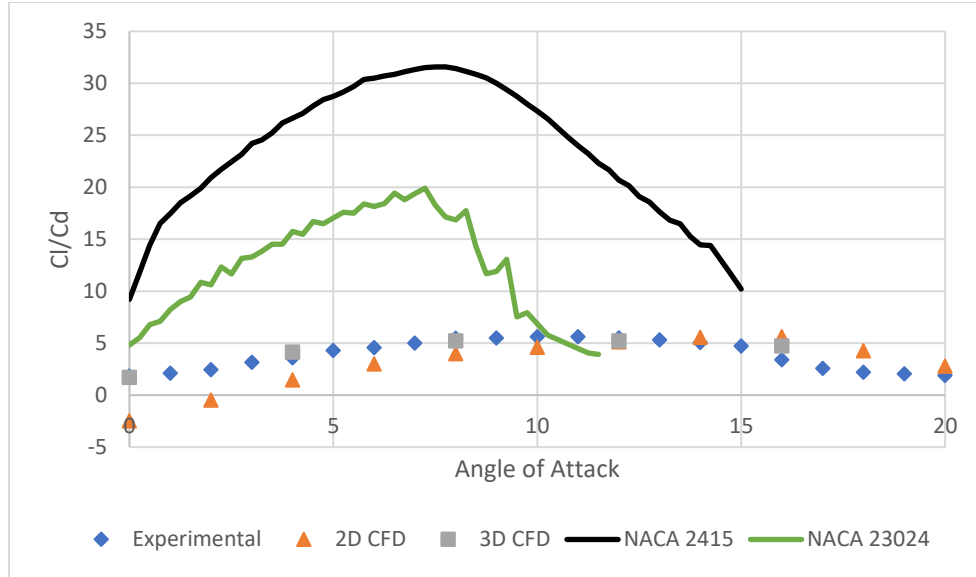


Figure 72: Lift to drag ratio vs angle of attack for all tests on CVCII and experimental data on select NACA airfoils

6.6. Performance score

With the results from the 2D CFD analysis, the performance score outlined in section 4 can be calculated. The integral is approximated by averaging every neighboring pair of Cl/Cd values, multiplying them with the change in AoA (two degrees), and summing them together:

$$\int_0^{20} \frac{C_L}{C_D} d\alpha \approx \sum_{i=1}^{19} \frac{\frac{C_L}{C_{Dn}} + \frac{C_L}{C_{Dn+1}}}{2} * 2$$

The value of the integral is 66.91. Dividing by the volume of 88cm^3 :

$$P_1 = \frac{66.91}{88} = 0.7603$$

From figure 37, the stall angle in the 2D CFD analysis is 16 degrees:

$$P_2 = \frac{\alpha_{stall}}{4} = \frac{16}{4} = 4$$

Making the total performance score:

$$P = 0.6(0.7603) + 0.4(4) = 2.056$$

Unfortunately, as there are no bonus marks for creativity, the final performance score of the CVCII airfoil is 2.056.

6.7. Sources of error

6.7.1 Experimental Errors

The roughness of the airfoil surface may have potentially introduced some error. The two sides of the airfoil were glued together, so some glue was pushed to the outer surface during assembly. Although the wing was sanded before the wind tunnel test, the glue was not fully removed. Additionally, the

finish of the 3D printed part was quite rough, and again, although it was sanded, the surface was not completely smooth. For comparison with the CFD analysis, a surface roughness value was added to the CFD portion of the project, but the correct surface roughness to match that of the 3D printed wing was unknown. The mount and the force transducer may have also affected the results. The force transducer was positioned right underneath the middle of the wing, so the flow may have been disturbed by its presence.

The zero angle of attack position was set by eye, so it is possible that it was set up incorrectly. This error would result in the same lift and drag curves, but they would be offset by the error in the zero angle of attack position.

The drift correction assumed that the sensor drift behaves linearly. Any deviations of the actual drift from this linear behavior would result in some error.

The way in which blockage was calculated may have also led to some small errors in the resulting lift, drag, and moment coefficients. The blockage was calculated assuming the wind tunnel area is reduced by the projection of the wing in the direction of the wind. It is likely that the resulting area blocked, especially at higher angles of attack, may be overestimated, resulting in lift and drag coefficients being lower than they should be.

6.7.2 CFD Analysis Errors

Discretization error due to the mesh size likely affected the results. For the 2D case specifically, the discretization error is low (on the order of 1%), as the lift and drag coefficients were not changing significantly as the mesh was being refined. For the 3D case however, the difference in lift coefficient between the finer and finest meshes was 7.4%. This implies that the mesh was far from converged and requires more elements. Unfortunately, this error could not be resolved due to the 512,000-element limit set on ANSYS Student.

Domain size can also contribute to errors in the CFD analysis; however, these errors are believed to be low (on the order of 1%) as guidelines from literature were followed.

There may be errors due to the models chosen for this analysis. Specifically, the turbulence model may introduce some error. While the k- ω SST model was deemed a good choice for this analysis, it is still a model and cannot perfectly predict turbulent flow behavior.

The use of a steady solver could also introduce errors. In the early stages of the project, the SIMPLE algorithm was producing unsteady, oscillating results. Although the unsteady results were fixed when switching to the coupled scheme, the unsteady SIMPLE scheme might imply that the case is inherently unsteady.

6.8. Improvements

6.8.1 Experimental

There are some improvements that could be made to the process of building the wing. When gluing the parts together, more care should have been taken to ensure as little glue as possible ends up on the surfaces of the wing. More time should have been taken to sand the wing to limit the effects of skin friction. Using a level to set the zero angle of attack point on the stepper motor would reduce the error due to the initial angle. Taking wind speed measurements around the cross section at which the wing is

placed could provide more insight on the extent to which blockage is affecting the wind speed, thus, resulting in more accurate lift and drag coefficient values.

6.8.2 CFD

Using a version of ANSYS that does not have the 512,000-element limit in place could greatly reduce the discretization error created by the large elements, specifically in the 3D case. A domain sensitivity study would provide more insight on the extent of errors due to the domain size. For the sake of saving time on this project, literature values were used instead of investigating the effect of domain size for this specific case. A transient study may also be valuable in determining the effect of any transient effects on the results.

6.8.3 Design

The wing itself has a lot of room for improvement. The profile shape allows the air to separate at the 0.55C location, leading to a decrease in lift and increase in pressure drag even at low angles of attack. There are most likely better car shapes to choose from if the profile must be shaped like a car. The bottom surface can use some improvements too. As seen in figure 62, a small bump was included in the profile when sketching the outline of the car. This bump is quite detrimental to the low angle of attack performance of the wing, specifically in the 2D CFD analysis.

In addition to changing the profile, the wing sweep could also use some improvements. Although the elliptical chord length distribution was used to minimize drag, the wing did not completely taper off to a zero-chord length at the wing tip. Instead, the tip chord length was reduced to 19.5mm. The choice to keep some chord length at the tip was made to ensure the print would not fail, as the wing would get quite thin if the chord length was reduced any further.

7. Conclusion

The new CVCII wing was modeled and tested experimentally in a wind tunnel, and numerically using CFD. The 3D CFD analysis and experimental test showed some agreement, but the 2D CFD analysis deviated from both. This was to be expected as the 2D CFD analysis does not capture finite wing effects that would affect the results of the 3D CFD or experimental case. The effect of finite wing effects becomes clearer when looking at the lift and drag characteristics of each test. The 3D CFD and experimental tests have a similar AoA at their maximum lift to drag ratio of ~11 degrees. The 2D CFD case has its maximum lift to drag ratio at an AoA of 16 degrees. This result highlights the fact that for finite wings the induced drag is proportional to the square of the lift coefficient as outlined in section 3.1. Another example of finite wing effects changing the lift and drag characteristics is in the slopes of the lift curves. The 2D CFD case has a lift curve slope that is almost two times greater than the experimental and 3D CFD lift curve slopes. This effect is likely caused by downwash changing the effective angle of attack in the finite wing cases.

The 2D CFD case was used to calculate the performance score of the CVCII. The resulting score was 2.056.

When comparing the performance of the CVCII to other conventional airfoils, it was found that the lift to drag ratio of the CVCII is quite poor. Although the lift vs AoA performance of the CVCII somewhat matches that of the NACA airfoils, the CVCII experiences much more drag. Most of the discrepancy in drag can be attributed to pressure drag acting on the CVCII. Because of the unconventional shape, the

flow does not stay attached on the top surface even at low angles of attack and separates at the rear window location. This separation creates a low-pressure zone that pushes to the left and does not overcome the high-pressure zone on the front half of the airfoil that pushes to the right. This difference in pressure leads to the high pressure drag experienced by the CVCII at all angles of attack.

Based on its performance, the CVCII is unlikely to be the wing choice for the new UAV. Although the lift coefficient is on par with other conventional airfoils, the drag is much too high and would require a large thrust to stay in flight. This issue becomes clearer when comparing the maximum lift to drag ratio of the airfoils. The maximum lift to drag ratio for the CVCII is 5.6, while the maximum lift to drag ratio of the NACA 2415 is almost 6 times higher, at 31.6. The CVCII did however provide an interesting analysis into an unconventional wing shape.

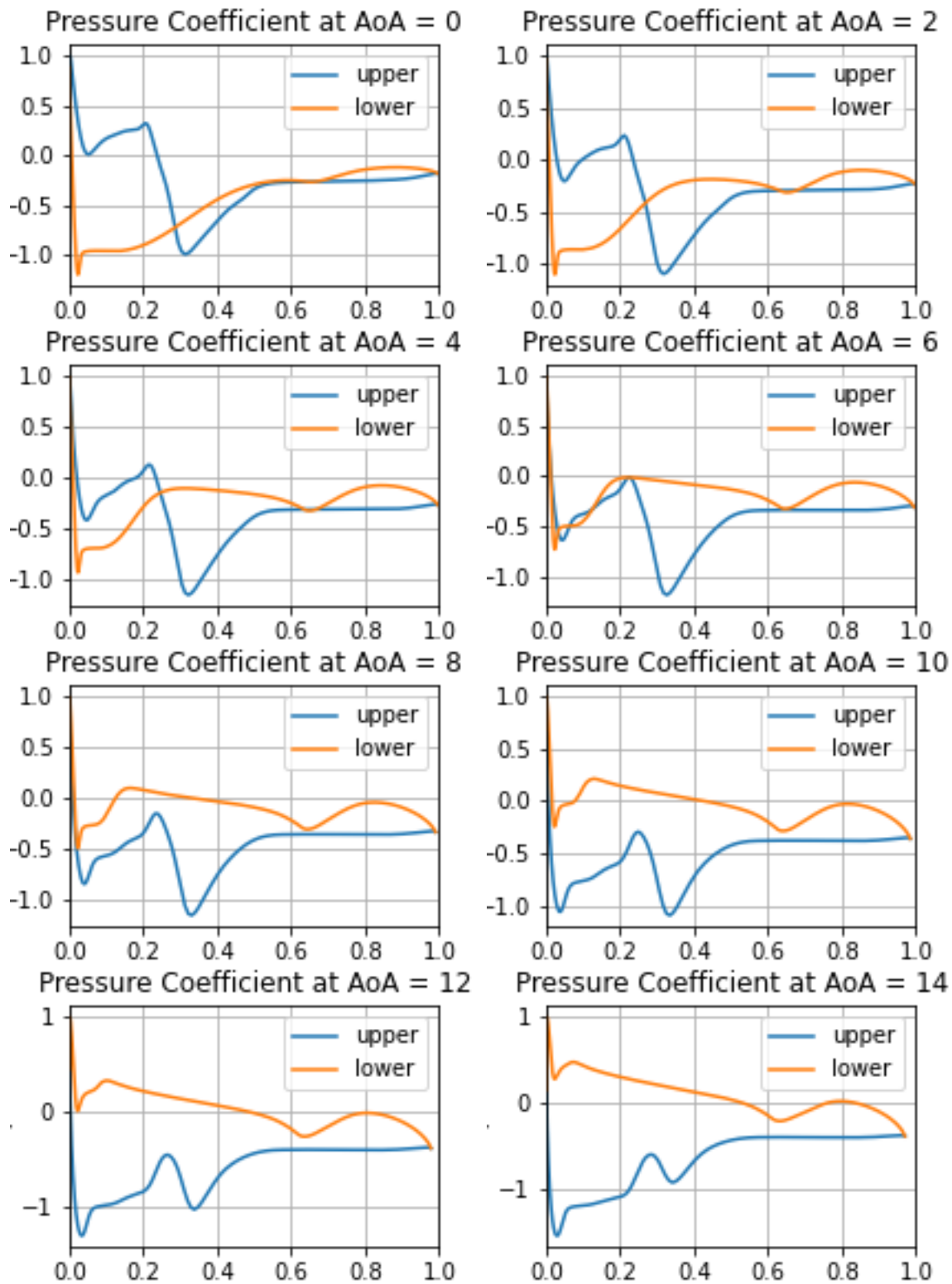
8. References

- [1] - Anderson, J., 2017. *Fundamentals of Aerodynamics*. 6th ed. McGraw Hill.
- [2] - Thecarconnection.com. 2021. *Image: 2005 Honda Civic Sedan EX AT SE Side Exterior View, size: 640 x 480, type: gif, posted on: December 7, 2009, 3:06 am - The Car Connection*. [online] Available at: <https://www.thecarconnection.com/image/100288366_2005-honda-civic-sedan-ex-at-se-side-exterior-view> [Accessed 13 December 2021].
- [3] - Airfoiltools.com. 2021. *Airfoil database search*. [online] Available at: <<http://airfoiltools.com/search/index>> [Accessed 9 December 2021].
- [4] - En.wikipedia.org. 2021. *Supermarine Spitfire - Wikipedia*. [online] Available at: <https://en.wikipedia.org/wiki/Supermarine_Spitfire#/media/File:Spitfire_mk2a_p7350_arp.jpg> [Accessed 13 December 2021].
- [5] - Drahmednagib.com. 2021. [online] Available at: <https://drahmednagib.com/CFD_2018/Fluent_Lecture_4_Fluent_Solver_Settings.pdf> [Accessed 13 December 2021].
- [6] - Dragonfly.tam.cornell.edu. 2021. [online] Available at: <<https://dragonfly.tam.cornell.edu/teaching/mae5230-cfd-intro-notes.pdf>> [Accessed 13 December 2021].
- [7] - Ghiroaga, C., 2021. *Lift and Drag for Symmetric and Cambered Airfoils*. [online] D2L. Available at: <<https://d2l.ucalgary.ca/d2l/le/content/399820/viewContent/4886111/View>> [Accessed 9 December 2021].
- [8] - Goetten, F., Finger, F., Marino, M. and Bil, C., 2019. A review of guidelines and best practices for subsonic aerodynamic simulations using RANS CFD. In: *Asia Pacific International Symposium on Aerospace Technology*. Victoria, Australia.
- [9] - Cfd-online.com. 2021. *SST k-omega model -- CFD-Wiki, the free CFD reference*. [online] Available at: <https://www.cfd-online.com/Wiki/SST_k-omega_model> [Accessed 13 December 2021].

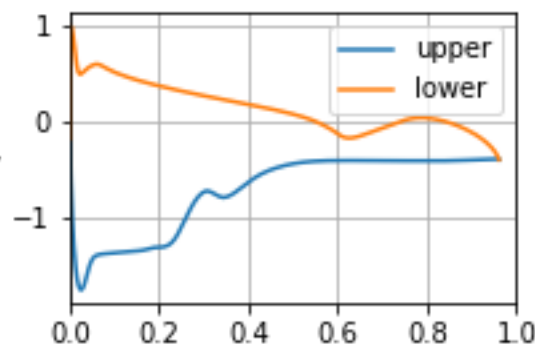
[10] - Engineeringtoolbox.com. 2021. *Air - Dynamic and Kinematic Viscosity*. [online] Available at: <https://www.engineeringtoolbox.com/air-absolute-kinematic-viscosity-d_601.html> [Accessed 13 December 2021].

[11] - Abbott, I. and Doenhoff, A., n.d. *Theory of Wing Sections*. [Place of publication not identified]: Dover Pubns

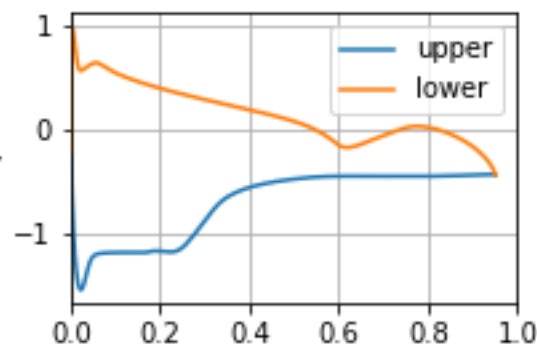
Appendix A: Pressure coefficient, skin friction coefficient, and boundary layer plots for 2D CFD



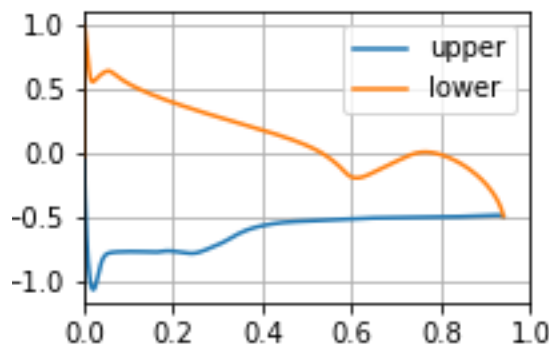
Pressure Coefficient at AoA = 16



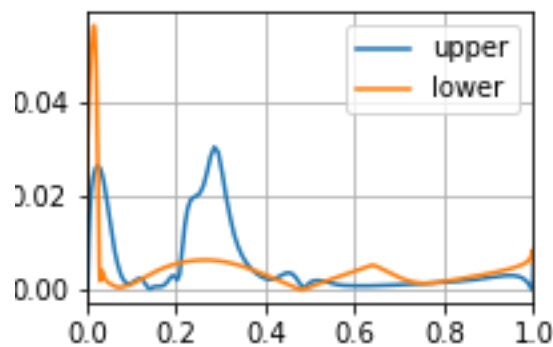
Pressure Coefficient at AoA = 18



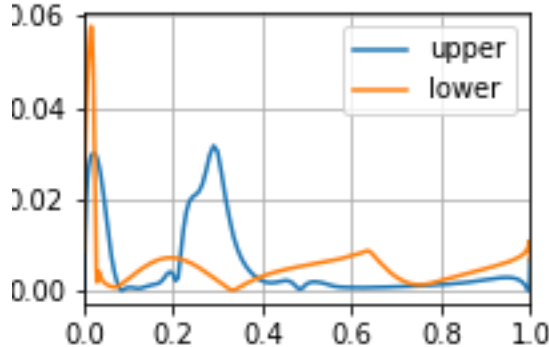
Pressure Coefficient at AoA = 20



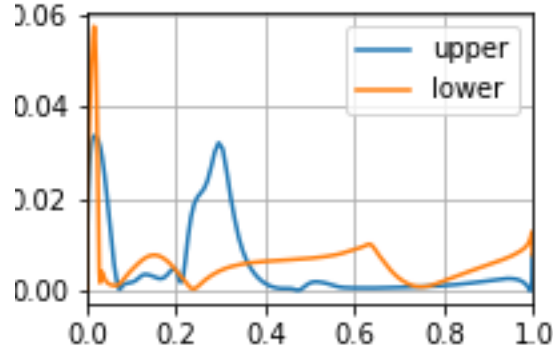
Skin Friction Coefficient at AoA = 0



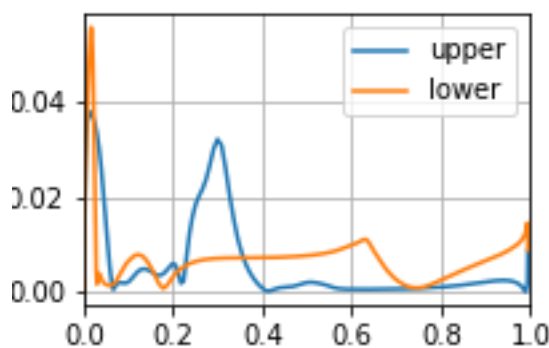
Skin Friction Coefficient at AoA = 2



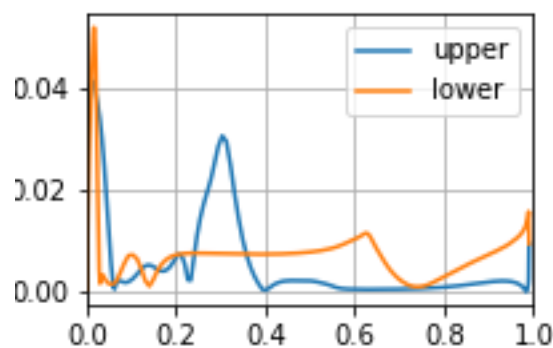
Skin Friction Coefficient at AoA = 4



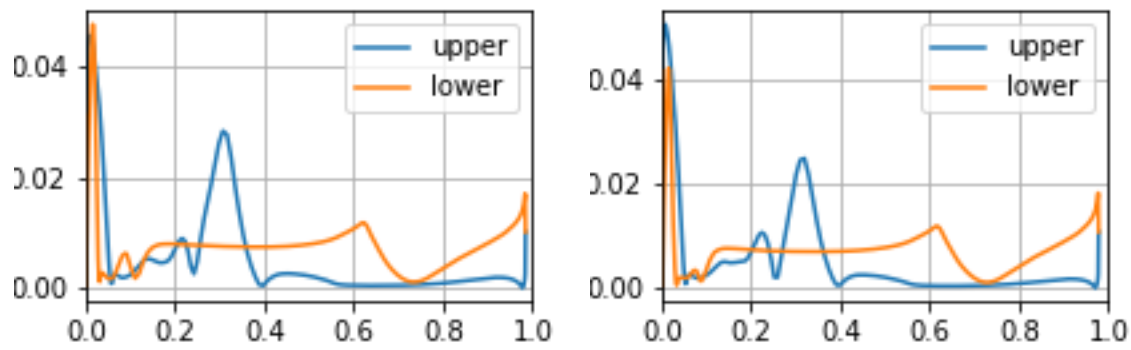
Skin Friction Coefficient at AoA = 6



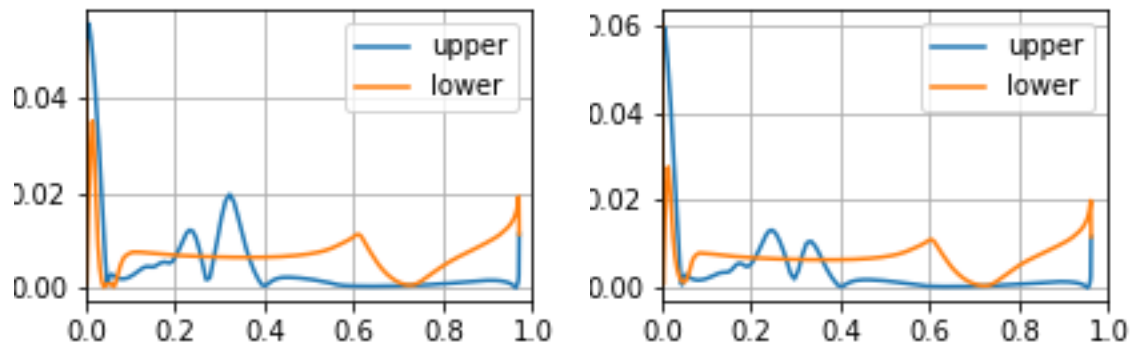
Skin Friction Coefficient at AoA = 8



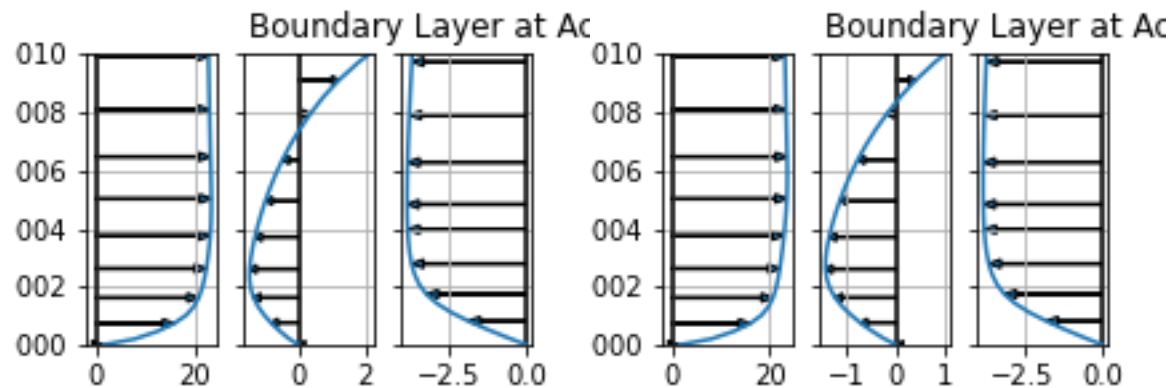
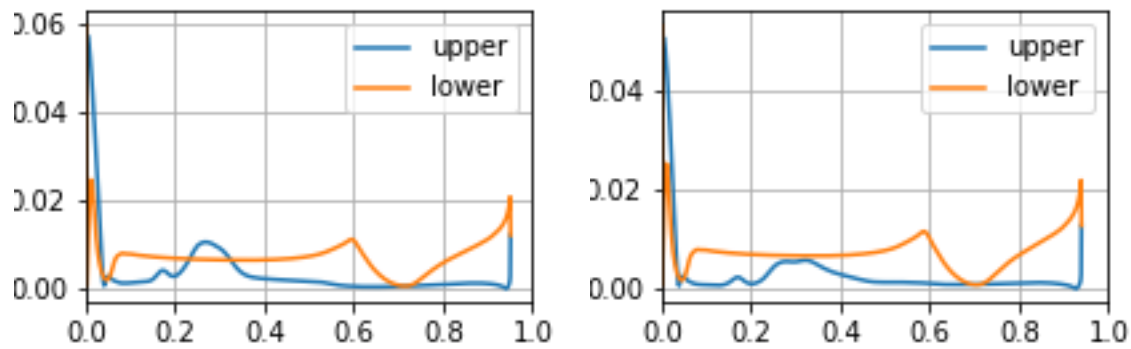
Skin Friction Coefficient at AoA = 10° Skin Friction Coefficient at AoA = 12°

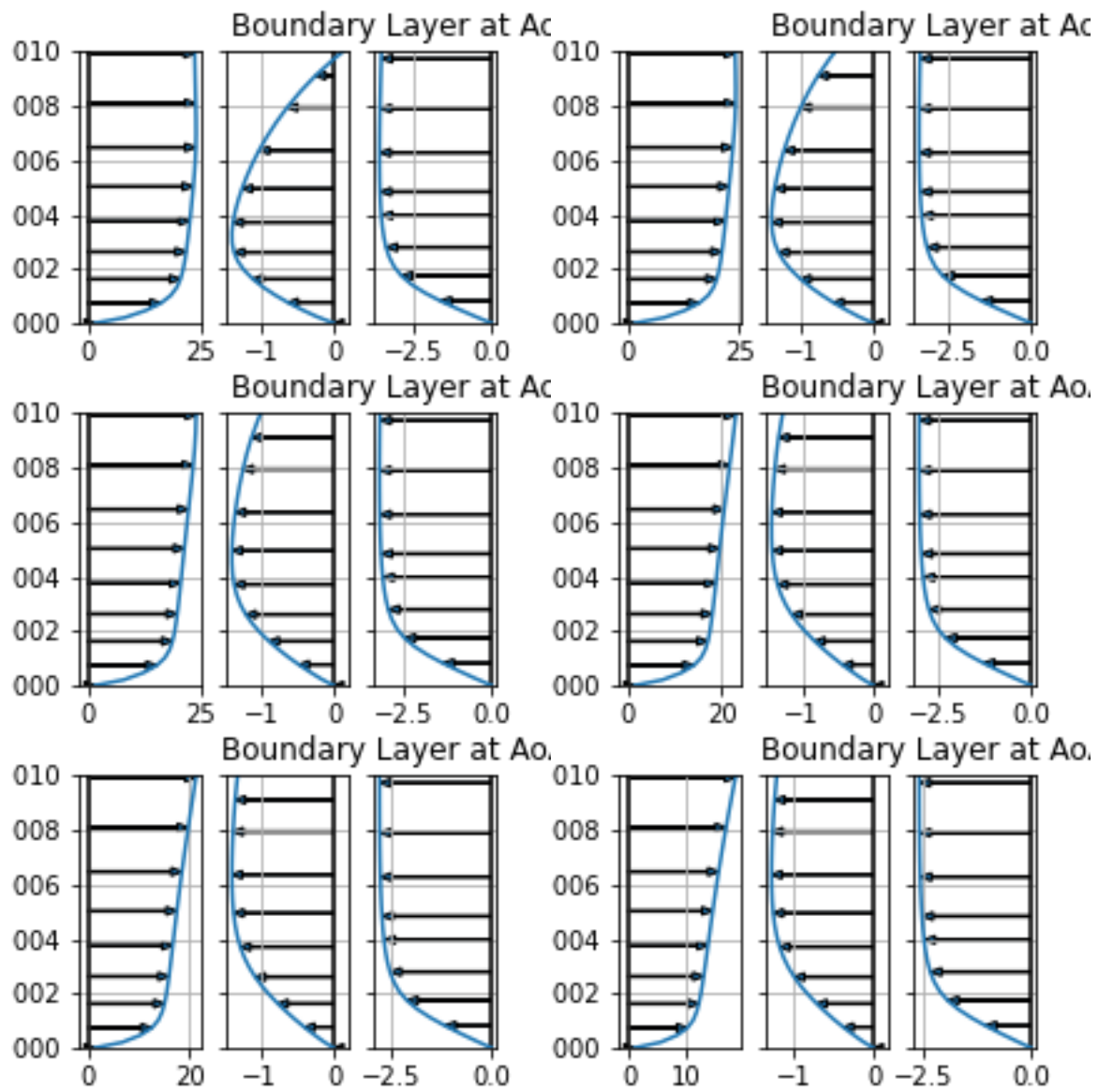


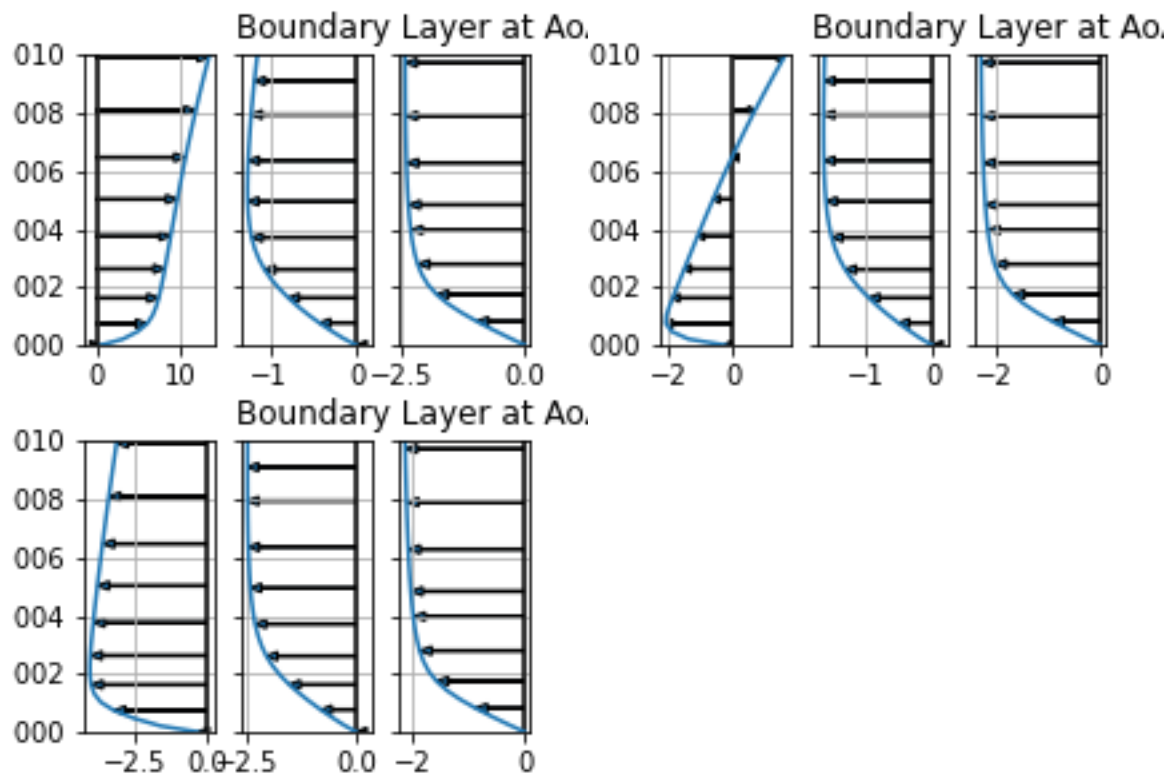
Skin Friction Coefficient at AoA = 14° Skin Friction Coefficient at AoA = 16°



Skin Friction Coefficient at AoA = 18° Skin Friction Coefficient at AoA = 20°







Appendix B: Spanwise pressure coefficient for 3D CFD analysis

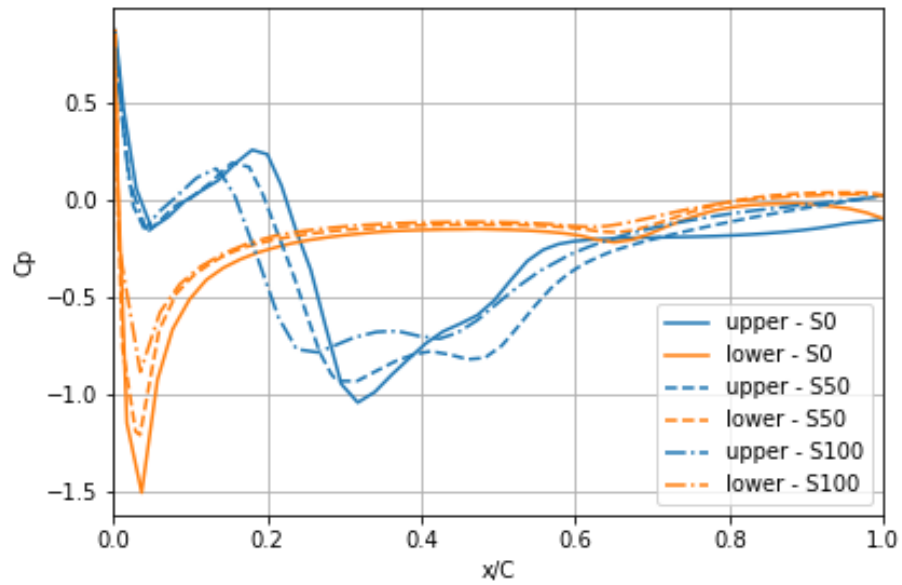


Figure B 1: Pressure coefficient at three spanwise locations for 3D CFD analysis at $AoA=0$

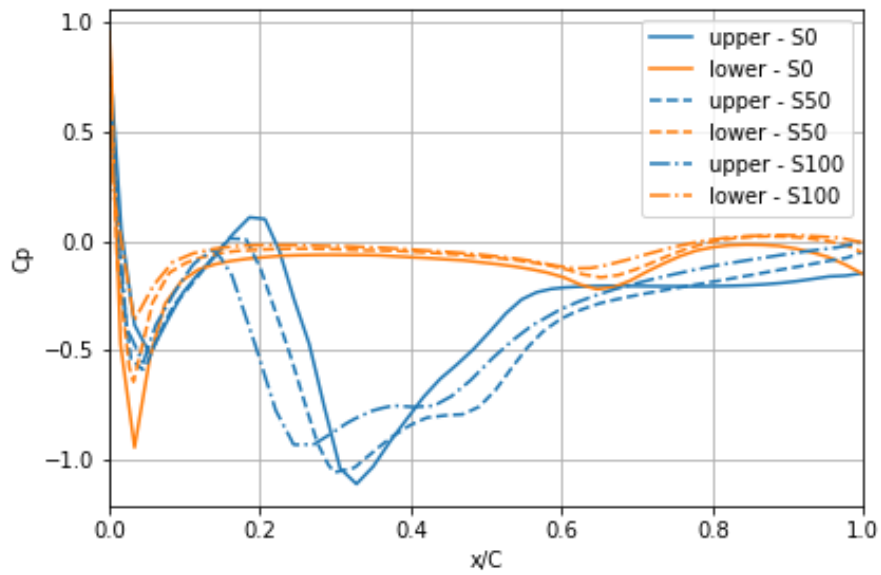


Figure B 2: Pressure coefficient at three spanwise locations for 3D CFD analysis at $AoA=4$

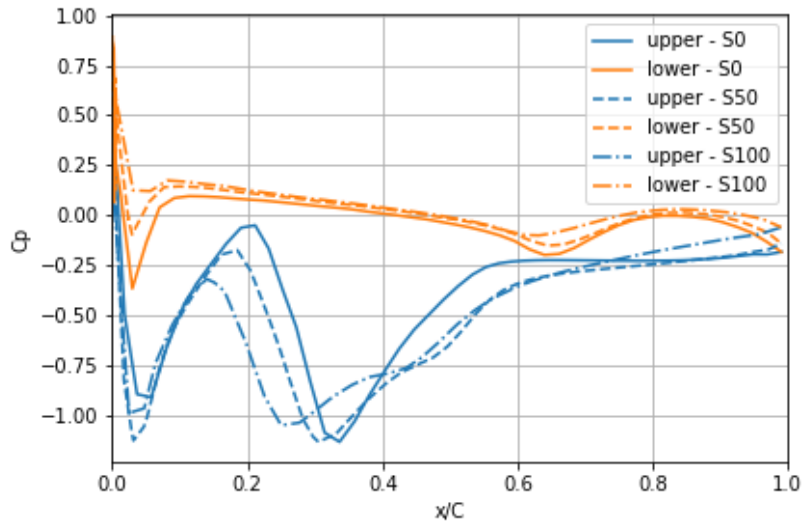


Figure B 3: Pressure coefficient at three spanwise locations for 3D CFD analysis at AoA=8

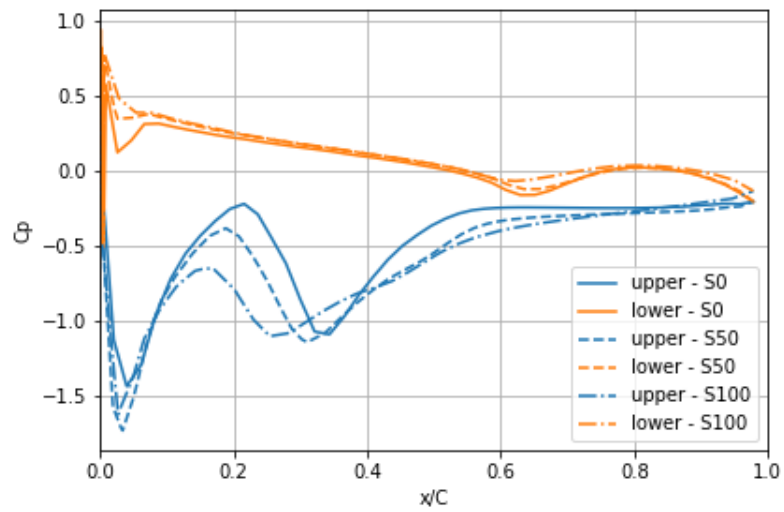


Figure B 4: Pressure coefficient at three spanwise locations for 3D CFD analysis at AoA=12

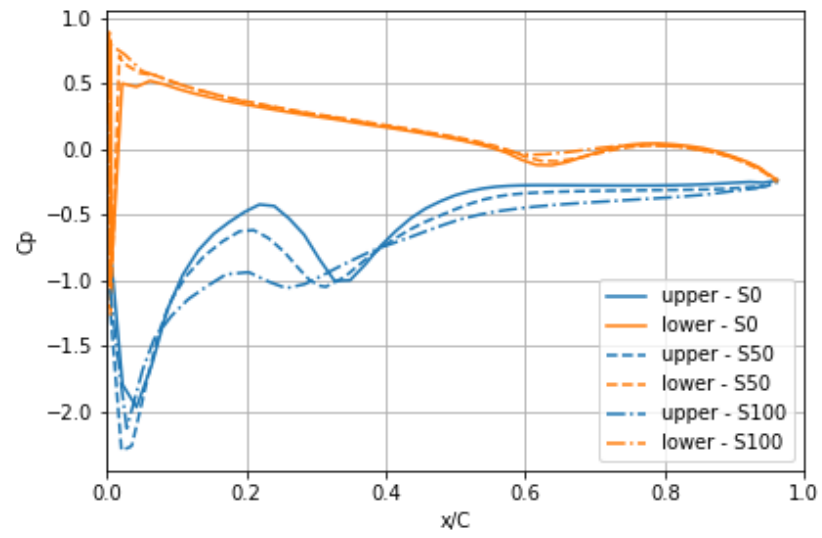


Figure B 5: Pressure coefficient at three spanwise locations for 3D CFD analysis at AoA=16